

Publication No. U-4045
W.O. 2386

APPLIED RESEARCH LABORATORIES

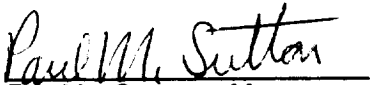
FINAL TECHNICAL REPORT
STUDY OF THERMAL RADIATION, PARTICLE IMPINGEMENT
HEATING, AND FLOW FIELD ANALYSIS OF SOLID
PROPELLANT ROCKET EXHAUSTS

Prepared for: George C. Marshall Space Flight Center
NASA
Huntsville, Alabama

Under Contract: NAS8-20276
Date of Contract: 30 December 1965
Contract Expiration Date: 28 February 1967

Date of Report: 19 April 1967

Prepared by: A. J. Laderman
W. C. Kuby
S. R. Byron
D. J. Carlson
C. D. Bartky

Approved by: 
P. M. Sutton, Manager
Physics Laboratory

PHILCO-FORD CORPORATION
Aeronutronic Division
Newport Beach, California

ABSTRACT

An engineering calculational procedure is described which is used to compute particle radiation and impingement damage to objects affected by the exhaust plume of solid propellant rocket motors. The approach adopted here is applicable to plumes of any optical depth. The measured optical properties of condensed phase material are used directly, which provides a much better description of the wavelength and temperature dependence than does the model assumed by Morizumi and Carpenter¹ or by Fontenot.²

Results of the calculation are compared with spectral and total radiation measurements made at a location near the exit plane of the SII ullage motor. The calculated equilibrium gas radiation represents 23% of the total measured radiation. The calculated particle radiation from Al_2O_3 ranges from 10.5% to 63% of the total measured radiation, the variation arising from uncertainties in (1) the optical properties of liquid Al_2O_3 in the far infrared, (2) the magnitude of the searchlight effect, and (3) the degree of supercooling in the nozzle and plume expansion. Recommendations for future studies are presented.

CONTENTS

SECTION	PAGE
1 INTRODUCTION	1
2 ANALYTIC FORMULATION	4
2.1 Two Phase Flow.	6
2.1.1 Gas Flow Field	6
2.1.2 Particle Trajectories.	8
2.2 Particle Optical Properties	12
2.2.1 Scattering and Absorption by Particles . . .	12
2.2.2 Particle Optical Data.	14
2.2.3 Cloud Optical Properties	17
2.3 Particle Plume Properties	18
2.3.1 Local Particle Size Distribution	18
2.3.2 Radiation Properties	21
2.3.3 Impingement Properties	21
2.4 Particle Plume Radiation.	22
2.4.1 Radiative Transfer in a Scattering, Absorbing, and Emitting Medium	22
2.4.2 One-Dimensional Beam Approximation	24
2.4.3 Power to the Detector.	26
2.5 Gas Radiation	27
3 RESULTS AND DISCUSSION	30
3.1 Plume Radiation	30
3.1.1 Experimental Results	30
3.1.2 Computation.	31
3.1.3 Discussion	33
3.2 Particle Impingement Effects.	44

SECTION	PAGE
3.2.1 SII Ullage Tests	44
3.2.2 Aeronutronic Tests	47
4 CONCLUSIONS AND RECOMMENDATIONS.	52
REFERENCES	54
ILLUSTRATIONS.	58

ILLUSTRATIONS

FIGURE	PAGE
1	Flow Chart of Calculation Scheme.
2	Absorption Coefficient and Index of Refraction of $\gamma\text{-Fe}_2\text{O}_3$
3	Imaginary Part of Refractive Index of Alumina
4	Particle Size Distribution for SII Ullage Motor
5	Illustration of Coordinate System for Radiative Transfer Problem.
6	Radiation Detector View Geometry.
7	Calculated Radial Pressure and Temperature Profile at Observation Station for SII Ullage Motor Plume.
8	Measured Radiation Heating Rates for SII Ullage Motor 6" from Exit Plane Using Model FF-1 Radiometer.
9	Particle Continuum and Gas Band Radiation for SII Ullage Motor; Theoretical Predictions Compared with OAL-NASA Experiments.
10	Polar Scattering Diagrams for Computation of \bar{f} for $2\pi r/\lambda = 0.5, 3.0$
11	Polar Scattering Diagrams for Computation of \bar{f} for $2\pi r/\lambda = 5, 10$
12	Fraction of Energy Incident on a Sphere which is Scattered into One Steradian Centered at 90° to the Incident Direction.

FIGURE

PAGE

13	Ratio of Scattered Light (Searchlight Emission) to Thermal Emission for Conditions of SII Ullage Motor Radiometer Measurement.
14	Flight Spectrum of Solid Propellant Booster
15	Ground Test Spectrum of Large Solid Propellant Booster

NOMENCLATURE

a	Constant in particle size distribution function
A	Area; Avogadro's number
A_m	Constant coefficient in Equation (2-31)
b	Constant in particle size distribution function
B	Blackbody function, radiant flux per unit area per unit wavelength
$B(T_{\text{eff}})$	Effective blackbody function defined by Equation (2-20)
c	Specific heat
c_p	Specific heat at constant pressure
C	Number fraction of particles of species i
C_D	Drag coefficient
C_m	Constant coefficient in Equation (2-31)
\bar{f}	Fraction of incident spectral radiation (on a particle) scattered at 90° into one steradian
F	Scattering function; spectral flux per steradian
F'	spectral flux
h	Planck constant; enthalpy
I	Radiation flux per unit area per unit wavelength interval
I^+	Radiation flux per unit area per unit wavelength interval directed toward detector along line of sight

I^-	Radiation flux per unit area per unit wavelength interval directed away from detector along line of sight
k	$= 2\pi/\lambda; \langle \sigma_a \rangle / (\langle \sigma_a \rangle + \langle \sigma_s \rangle)$; rate constant; thermal conductivity
K	Constant defined in Equation (3-17)
K_D	Ratio of drag coefficient to Stokes' drag coefficient, Equation (2-8)
K_H	Ratio of Nusselt number to Stokes' Nusselt number, Equation (2-9)
$K.E.$	Particle kinetic energy flux defined by Equation (2-21)
L	Heat of fusion
m	Complex index of refraction, $m = n_1 - n_2 i$
M	Mach number; molecular weight
n_1	Real part of complex index of refraction
n_2	Imaginary part of complex index of refraction
N	Number density
Nu	Nusselt number
P_d	Power received by radiation detector
Pr	Prandtl number
q_c	Theoretical convective heating rate
q_R	Theoretical radiative heating rate
q_{tot}	Total stagnation heating rate
q_{TME}	Total stagnation heating rate measured experimentally
q_{PEE}	Particle impingement heating rate $= q_{TME} - q_R - q_c$
q_{TPE}	Sum of theoretical particle thermal and kinetic energy flux

q_{TTE}	Theoretical particle thermal energy flux
q_{TKE}	Theoretical particle kinetic energy flux
Q	Optical efficiency factor = $\sigma/2\pi r_p^2$
r	Reflectivity
r_p	Particle radius
\dot{r}	Surface regression rate
R	Radius of curvature; distance from scattering particle
Re	Reynolds number
t	Time; transmissivity
T	Temperature
T_{eff}	Effective temperature defined by $B(T_{eff})$
$T.E.$	Particle thermal energy flux defined by Equation (2-22)
v_p	Particle velocity
v_g	Gas velocity
w	Power emitted per unit volume
x	Axial coordinate; optical parameter = $2\pi r_p/\lambda$
X	Mole fraction
y	Radial coordinate
$\langle \rangle$	Denotes local value averaged over particle size

Greek

α	Coefficient of particle momentum equation defined by Equation (2-3); radiation interaction factor, see Equation (2-7); absorption coefficient; accommodation coefficient
β	Fraction of light scattered in backward direction
γ	Ratio of specific heats

$\bar{\gamma}$	Effective specific heat ratio for equilibrium gas-particle mixture
$\gamma(\theta)$	Angular scattering distribution function defined by Equation (2-24)
δ	Surface regression
Δ	Denotes increment in quantity
ϵ	Emissivity
η	Thermal diffusivity
θ	Direction of scattered light from incident beam; steady state ablation time
K	Constant defined by Equation (2-32)
λ	Spectral
μ	Viscosity; $\cos\chi$
μ'	Running variable over values of μ
μ^*	Line of sight coordinate, see Equation (2-36)
ν	Frequency of emitted radiation
ξ	Angle between normal to detector area and line of sight
ρ	Density
σ	Optical cross section
τ	Optical thickness defined by Equation (2-32)
τ_{th}	Transmissivity of particle cloud between nozzle throat and measuring point
\emptyset	Azimuthal angle; ratio of particle to gas mass flow rates
\emptyset'	Running variable over values of azimuthal angle
\emptyset^*	Line of sight coordinate, see Equation (2-36)
Φ	Skew-symmetric particle size distribution function
χ	Zenith angle

χ'	Incident zenith angle
ω	Solid angle
ω_{th}	Solid angle subtended by particle from nozzle throat plane
Ω_d	Solid angle viewed by detector

Subscripts

a	Absorption
aw	Adiabatic wall
A,B	Atomic species
ch	Chamber
d	Detector
e	Exit plane
em	Emission
ext	Extinction
g	Gas
i,j,k	Numeric index
l	Liquid
L	Limiting streamline
m	Index parameter for equivalent isothermal slabs, see Equation (2-31)
max	Maximum
min	Minimum
n	Plume boundary farthest from detector
o	Initial; plume boundary nearest detector; centerline
p	Particle

r_p	Particle radius
s	Scattering; solid; stagnation
se	Searchlight
t	Total
th	Nozzle throat
w	Wall
x	Axial location
y	Radial location
∞	Freestream
λ	Spectral

SECTION 1

INTRODUCTION

This report describes the results of a 12-month study conducted for NASA Huntsville under Contract NAS8-20276, which has the objective of developing an engineering calculational procedure for problems concerned with the thermal environment of solid propellant rocket exhaust plumes over a range of altitudes. The major considerations of such an environment include nozzle and plume two-phase flow phenomena, particle cloud radiative properties, and particle impingement heating and erosion damage. These effects are of practical concern since the exhaust plume of a solid propellant motor may impinge upon or radiate to nearby objects, such as stages undergoing separation, fins and surfaces located near boost support rockets, or spacecraft subjected to the plume of a nearby thruster. The condensed phase material which is present in the plume exhibits high radiative emissivity and considerable thermal lag which enhance radiation from the plume. In addition, particle impingement results in a high heat transfer rate to the affected surfaces and may produce significant erosion of protective coatings.

The overall problem may be divided into three phases: (1) nozzle two-phase flow effects, required as input for subsequent exhaust plume

calculations, (2) two-phase plume gasdynamic and radiative behavior and (3) resultant effects of the plume properties on the structure of interest.

The general nature of two-phase nozzle flow has been well studied and adequate theoretical and experimental information is available to predict effects for given size particles. Computer programs are available to calculate the gas flow field through the nozzle and the particle trajectories and temperatures. The major uncertainty at the present time is knowledge of the actual particle size distribution prevailing in specific rocket motors.

Beyond the nozzle exit, the gas-particle cloud expands to form a two-phase plume. Aspects of the gas plume for which analytical methods and computer programs are available include the structure of the flow within the shock bottle (method of characteristics solutions are available), the distance to the normal shock wave which is characteristic of the single nozzle plume, the plume maximum diameter and radius of curvature near the nozzle exit, and the afterburning interface between the exhaust and ambient gases. Aspects of the particle plume which have been studied include the distance to the normal shock, the two-phase flow properties in the vacuum plume or shock bottle (treated with both coupled and uncoupled analyses), and far field particle plume temperatures and velocities. In general, it can be said that the particle plume may be calculated to within the accuracy for which the gas plume is known and, at high altitudes, where the particle plume is highly decoupled from the gas plume, the entire particle plume may be calculated.

Since the gas and particle plume flow field structure can be determined with existing techniques, major emphasis in the present work was directed toward development of a calculation procedure for predicting two-phase plume radiation. The method evolved has been divided into two separate computer programs. The first portion of the radiative program evaluates the local average radiative properties of the plume, based on a knowledge of the plume flow field and the optical properties of the individual particles. Optical properties for Al_2O_3 , the most common

particulate matter in the plume, were calculated by Mie theory for a wide range of temperature, wavelength, and particle size, and are stored on cards which are integral with the computer program. This program also calculates the local average thermal and kinetic energy flux of the particles which is used in the analysis of particle impingement effects.

The second portion of the radiative computer program integrates the spectral radiative flux to a given target along arbitrary "lines of sight" between the target and the plume. The total flux to the target can then be determined by summation over all lines of sight and over the wavelength interval of interest.

Initially it was assumed that gas phase radiation would be negligible compared to the particle continuum. However during the course of the program it was discovered that under certain conditions the gas contribution can constitute a significant fraction of the total radiation. Since, in the example calculation described later, the plume was optically thin, the gas radiation could be hand calculated and this contribution has been included in the final result. However, incorporating the gas calculation scheme into the current program, particularly for optically thick plumes, requires further study.

A test calculation of the computer program was performed for the SII ullage motor. This motor was selected since experimental measurements of total and spectral plume radiancy were available for comparison with theoretical results. In addition, an analysis of particle impingement heating effects, based on experimental data obtained from models located in the SII ullage plume, was performed and the results compared with those obtained from similar tests conducted in the Aeronutronic two-phase cold flow facility.

The theoretical calculation of plume radiation, particularly the spectral radiancy, was in qualitative agreement with experimental measurements. Major sources of the discrepancy between theory and experiment have been delineated, on which basis programs for future work are recommended.

SECTION 2

ANALYTICAL FORMULATION

This section presents a detailed description of the analytical technique developed under this contract for calculation of radiative and impingement heat fluxes from a two-phase plume. Due to its complexity and length, the overall computational procedure has been subdivided into a number of separate sub-routines. This minimizes machine storage problems and allows the opportunity for intermediate engineering decisions.

The calculation scheme is shown in the Flow Chart of Figure 1, where the circled quantities represent input data and the boxed items indicate calculation routines. For a given propellant system and chamber pressure, the thermochemical calculation is used to determine the temperature and species concentrations in the chamber and the variation of these quantities during the expansion. This information, together with a specified nozzle geometry, provides the input for computation of the gas flow field. With these results, the particle trajectories, together with local velocities and temperatures, are determined and serve as input for calculating the particle plume structure, in terms of local particle number density and size distribution. From these, the local average radiative properties of the plume and local impingement energy

flux can be evaluated. Finally, the radiative transfer equation, simplified by appropriate assumptions, is integrated along "lines of sight" and the total flux to the target is determined by summation over the several lines of sight.

The thermochemical calculation routine and the supersonic gas flow field routine are currently available in the Lockheed-Huntsville method of characteristics program. Details of this program can be found in Reference 3 and are not supplied here. For convenience, this program will be referred to in subsequent paragraphs as the Lockheed program. The remaining programs, developed under this contract, will be referred to as follows:

<u>Program Designation</u>	<u>Program Title</u>
A	Particle Plume Structure
B	Particle Plume Properties
C	Particle Plume Radiation

As stated earlier, it was found that for the lightly loaded SII ullage motor considered here, radiation from the gas species contributed a significant portion of the total plume radiation. Since, in this instance, the plume was optically thin, it was possible to determine the gas contribution by hand calculation and the total radiation by summation of the gas and particle plume contributions. This is indicated in the flow chart of Figure 1.

Finally it should be pointed out that the radiation calculations described above are performed for each wavelength of interest. Consequently this procedure allows determination of both the total radiative flux and its spectral distribution.

In the following paragraphs, each of the calculation subroutines is described in detail.

2.1 TWO PHASE FLOW

2.1.1 GAS FLOW FIELD

Program A first completes the nozzle and plume gas flow field calculations before computing the particle trajectories. The subsonic and transonic flow regions are computed by using an approximate two-dimensional, axi-symmetric program. This program, described in detail in Reference 4, computes the gas flow field for an equilibrium gas-particle mixture with a constant effective specific heat ratio, $\bar{\gamma}$, and constant molecular weight. The gas velocity is computed from one-dimensional equations and assigned a position dependent velocity vector. That is, the gas is assumed to flow parallel to the wall at the wall, and parallel to the axis at the axis, and at an angle between these two found by linear interpolation at intermediate points using the radial position as the independent variable. To account for the non-axial velocity vector component, an axi-symmetric correction to the mass flow is applied to the continuity equation. For small angles of convergence or divergence this method is essentially a source flow determination.

The above axi-symmetric program can also be used to describe the supersonic flow in the nozzle and the plume expansion. In order to use this program to describe the plume flow field, an approximate Mach number distribution along the flow axis can be predicted by methods outlined by Hill and Habert.⁵ Using these centerline results, a fictitious nozzle can be generated that will yield the proper axial plume Mach number variation. Affixing this fictitious nozzle to the exit of the real nozzle allows the continuation of the 2-D program throughout the entire flow field.

It is recommended that, rather than using this over-simplified 2-D approximation throughout the flow field, a method of characteristics solution be used to describe the flow field in the plume region. In general, it appears that the approximate 2-D program is adequate for conical exit cones, but for bell shaped contours the method of characteristics program is superior and should be used even for the nozzle expansion flow. The

supersonic gas flow field in the rocket nozzle and in the plume can be computed using the existing Lockheed program. Equilibrium reacting gas solutions are provided by the NASA/Lewis Thermochemical Program whose output for several standard propellant systems has been stored on a master tape. The tape, which has provisions for including other propellants, has been incorporated in the Lockheed method of characteristics program, and gases of interest are introduced into the characteristics program by proper identification.

For the computations that are presented here the Lockheed method of characteristics program was used to generate the plume flow fields only; the approximate axi-symmetric 2-D program was used for the complete nozzle flow. The various flow properties resulting from either the two-dimensional program or the method of characteristics program are stored in an orthogonal mesh for use in computing the particle trajectories. By using a combination of programs, one can obtain constant γ solutions to the throat and constant γ , frozen, or equilibrium solutions from the throat on.

Since the characteristic output is along characteristic lines and the required gas flow field must fit a rectangular mesh for use in the particle trajectory routine, a program is included to make the proper conversion of the data. The intersection of the characteristic lines with lines of constant x , axial location, are found and the gas properties at these intersection points are determined by interpolation along the respective characteristic lines. The resulting gas properties mesh is then at irregular values of y , radial location, but on lines of regular values of x . Rather than either curve-fit or perform additional interpolations to make the y spacing regular, a four-point interpolation subroutine is used in the particle trajectory program so that the above irregular spacing can be accepted.

The gas flow field is computed without regard to the non-equilibrium effects resulting from particle lag. Actually, the gas and particle flow equations should be solved simultaneously as has been done by Kliegel.⁶ The coupling of the two flows, in essence, accounts for the

effects of body forces, dissipation, and heat exchange between the particles and the gas, making the local gas state dependent upon the behavior of the particles. The necessity of using a coupled flow description has been investigated by comparing the results obtained using a simpler, uncoupled method with those reported by Kliegel.⁶ It was found that, for moderate particle loadings or for flows in which the particle lag is minimal, the uncoupled solution is in agreement with the more detailed coupled solutions to well within the error introduced by other uncertainties such as nozzle internal shock waves, gas transport properties, particle size distribution, etc. Thus, except for unusually high particle loadings or large particle lags, it is recommended that an uncoupled solution be used for these calculations. A more detailed discussion of the assumption of uncoupled flows is found in Reference 7.

2.1.2 PARTICLE TRAJECTORIES

The independently determined gas flow field is stored in a rectangular mesh and the particle trajectories are computed using these flow field results. The particle momentum and energy equations are integrated using a modified Euler technique and a 4-point interpolation routine to determine the gas properties from the stored mesh. The drag and heat transfer coefficients take into account inertial, compressibility, and rarefaction effects as discussed in Reference 8. Any number of particle sizes can be computed and one has the option of computing a centerline, a limiting streamline, or any number of streamlines intermediate to the two limiting cases.

The momentum and energy equations for the particles are given in Reference 9. In this computing scheme the momentum equations are written in difference form as follows:

$$v_{p_{x_{i+1}}} = v_{p_{x_i}} + \left(\frac{\alpha_i + \alpha_{i+1}}{2} \right) [v_{g_{x_i}} + v_{g_{x_{i+1}}} - (v_{p_{x_i}} + v_{p_{x_{i+1}}})] \frac{\Delta t}{2} \quad (2-1)$$

$$v_{p_{y_{i+1}}} = v_{p_{y_i}} + \left(\frac{\alpha_i + \alpha_{i+1}}{2} \right) [v_{g_{y_i}} + v_{g_{y_{i+1}}} - (v_{p_{y_i}} + v_{p_{y_{i+1}}})] \frac{\Delta t}{2} \quad (2-2)$$

where

$$\alpha = 0.417 \times 10^{12} \frac{K_D \mu_g}{\rho_p r_p^2} \quad (2-3)$$

The computation is started by assuming that the particles are in equilibrium with the gas velocity and temperature in the chamber region. The integration time step is chosen as the smaller of two time increments which are computed as the time required for the particle velocity to change by a given fraction of its local value and a maximum time step equal to the time for the particle to go a given distance. Both of these controls are inputs to the program. In general, the first criterion is used throughout the nozzle, but the second becomes dominant in the plume region.

Since the particle lag relaxation time varies inversely with the particle radius, the minimum time step can exceed the relaxation time for the small particles, which exhibit small lags in regions where the gas velocity is relatively constant. Reducing the time step for such regions leads to excessive computer time so that an alternative solution has been used for these cases. If the computed minimum time step is greater than the particle relaxation time, defined by the time required for the particle to accelerate to $v_{g_{x_{i+1}}}$, the particle is assumed to be

in equilibrium with the gas and its velocity and temperature set equal to the gas values. It appears that no significant inconsistency is introduced by this assumption and the error, which has been demonstrated by comparison of approximate computations with those using reduced time steps, seems well within the engineering requirements.

The new location of the particle for the time step determined is computed from the following equations:

$$x_{i+1} = x_i + (v_{p_{x_i}} + v_{p_{x_{i+1}}}) \frac{\Delta t}{2} \quad (2-4)$$

$$y_{i+1} = y_i + (v_{p_{y_i}} + v_{p_{y_{i+1}}}) \frac{\Delta t}{2} \quad (2-5)$$

The gas flow field properties are determined from the input mesh at this new position. These gas properties and the initial particle properties are then averaged in the numerical particle momentum equations and the new particle velocities are computed. This is repeated until the change in location for successive iterations is less than an input criterion. The particle temperature is then computed using the following equation:

$$T_{p_{i+1}} = T_{p_i} + \left[\left(\frac{dT_p}{dt} \right)_i + \left(\frac{dT_p}{dt} \right)_{i+1} \right] \frac{\Delta t}{2} \quad (2-6)$$

where

$$\frac{dT_p}{dt} = - \frac{.914 \times 10^6}{r_p \rho_p c_p} \left[\frac{.305 \times 10^6 \mu_g c_p K_H}{Pr r_p} (T_p - T_{aw}) + .476 \times 10^{-12} \alpha \epsilon T_p^4 \right] \quad (2-7)$$

The program allows for the option of freezing the particle temperature at a specified temperature (fusion point) until the heat of fusion has been removed. This option simulates the equilibrium solidification of a liquid particle.

In the case of a limiting streamline computation the particle is assumed to start at a position of .95 times the chamber radius and is given the gas velocity at that point parallel to the nozzle axis. The particle trajectory is continued until either the particle passes beyond the wall, thus indicating an impaction, or the particle goes beyond the throat location. In the former case, the particle trajectory is re-started back at $x = 0$ and at a y position that is .95 times the previous particle starting point. In the latter situation, the particle trajectory is restarted at $x = 0$ but at a y position that is halfway between the

previous value of y and the largest value of y that has been computed previous to this. By this method, the maximum radial position for a given particle size is determined for which the particle will go through the nozzle without impacting on the nozzle wall. When this location has been determined, the particle trajectory starting at that point is then computed throughout the gas flow field.

If intermediate trajectories are required between the axial streamline and the limiting streamline this can be accomplished by inputting the number of intermediate trajectories required. The value of the starting point for the limiting streamline is then divided by the number of intermediate streamlines and trajectories computed from the starting points.

In order to use the above integration techniques properly, the correct drag and heat transfer coefficients must be used. Frequently Stokes' drag law alone or Stokes' drag law corrected for inertial effects has been assumed. This may be appropriate for certain regions but for nearly any under-expanded plume and for most supersonic exit cones, Stokes' law may be in gross error. Properly, Stokes' law corrections should take into account rarefaction and compressibility effects as well as inertial effects. Such corrections to the Stokes' law values have been included in this computer program. The values of the drag coefficient and heat transfer coefficients are found by multiplying the Stokes' values by K_D and K_H , respectively (see Equations (2-3) and (2-7)). The values of K_D and K_H are given as follows:

$$K_D = \frac{C_D}{C_{D_{\text{Stokes}}}} = \frac{[1 + 0.15 \text{Re}^{0.687}] [1 + e^{-(0.427/M^{4.63}) - (3.0/\text{Re}^{0.88})}]}{1 + (M/\text{Re})(3.82 + 1.28e^{-1.25 \text{Re}/M})} \quad (2-8)$$

$$K_H = \frac{N_u}{2} = \frac{1}{2} \left[\frac{2 + 0.459 \text{Re}^{0.55}}{1 + 3.42 (M/\text{Re})(2 + 0.459 \text{Re}^{0.55})} \right] \quad (2-9)$$

A detailed description of the development of these expressions is found in Reference 8. It is also noted in the energy equation for the particles

that the individual particle emissivity is required. In general, the convective flux from the particles to the gas dominates the particle temperature throughout the nozzle; however, in the plume the convective flux usually becomes negligible and the only method of particle cooling is by radiation. The value of the particle emissivity used in these calculations is based upon the optical data compiled by Carlson.¹⁰

In summary, the particle trajectory program allows the computation of particle trajectories, velocities, and temperatures given the propellant characteristics, ambient conditions and nozzle contour. In this program the subsonic and transonic flow fields are computed using an approximate two-dimensional routine and the supersonic and plume flow fields by the approximate two-dimensional routine or by the Lockheed method of characteristics program. The gas flow field is computed without regard to the non-equilibrium character of the particle flow and it is stored in an orthogonal mesh for use in all the trajectory calculations. The particle momentum and energy equations are integrated using a modified Euler technique and a four-point interpolation routine to determine the gas properties from the stored mesh. The drag and heat transfer coefficients take into account inertial, compressible, and rarefaction effects and the resulting trajectories, velocities, and temperatures are punched on cards for use in subsequent programs. Any number of particle sizes can be stacked and the program includes the option of computing centerline, limiting streamline, or any number of arbitrary intermediate streamline cases.

2.2 PARTICLE OPTICAL PROPERTIES

2.2.1 SCATTERING AND ABSORPTION BY PARTICLES

A beam of light which traverses an inhomogeneous medium is attenuated, a process called extinction, both by scattering of the light into other directions and by absorption. At a distance R from the scattering particle, the scattered light has the character of a spherical

wave. The direction of the scattered light is characterized by the angle θ with the direction of the incident beam, and by the azimuthal angle, ϕ . The scattered intensity may be written in the form:

$$I = I_0 F(\theta, \phi) / k^2 R^2 \quad (2-10)$$

where $k = 2\pi/\lambda$ is the wave number, and F is a dimensionless function of the direction of the scattered light. If the total energy scattered is equated to the energy incident on an effective area, σ_s , we have, using the preceding equation:

$$\sigma_s = (1/k^2) \int F(\theta, \phi) d\omega \quad (2-11)$$

where $d\omega = \sin\theta d\theta d\phi$ and the integration is performed over all directions. Similarly, the energy absorbed by the particle may, by definition, be put equal to the energy incident on an area, σ_a , and the total energy removed from the beam set equal to that removed by an area, σ_{ext} , where, from the principle of conservation of energy

$$\sigma_{ext} = \sigma_s + \sigma_a \quad (2-12)$$

At a given wavelength, the scattering and absorption cross sections of a spherical particle of homogeneous composition depend on only two parameters, the ratio of particle circumference to wavelength, $x = 2\pi r_p / \lambda$, and the complex index of refraction $m = n_1 - in_2$. For spherical particles of arbitrary size, the angular and total scattering cross section and the extinction cross section can be determined from Mie theory.¹¹ The absorption cross section is then obtained by subtraction. In general, a digital computer must be used to evaluate these quantities, although there are several simple limiting expressions for particles much smaller than the wavelength (Rayleigh scattering) and for those much larger than the wavelength (geometrical optics). The typical Al_2O_3 particle in the rocket plume requires the full expressions derived from the Mie theory. The computer program "Mie Scattering"¹² performs the computations of σ_s , σ_a , and β (the fraction of light scattered in a backward direction) for each

combination of the input parameters, r_p , the particle radius, T_p , the particle temperature, and λ , the wavelength. The input to the Mie program is found initially in a simple program called "PUNCH"¹³ which includes a table of the real and imaginary parts of the index of refraction of the particulate material as a function of λ and T_p , and outputs a set of cards containing the combinations r_p , T_p , and λ , together with the appropriate values of $n_1(\lambda, T_p)$ and $n_2(\lambda, T_p)$. The output of the Mie program, in the form of σ_a , σ_s , and β as a function of r_p , T_p and λ , has been stored on cards for use in Program B.

2.2.2 PARTICLE OPTICAL DATA

It is generally assumed that continuum radiation from an aluminized solid propellant motor can be attributed entirely to the alumina formed during the combustion process. For the SII ullage motor, however, the alumina content is only 7.8% while approximately 2% of Fe_2O_3 , which is used as a burn rate controller, is also present.

A literature search on the optical properties of iron oxide was made. Since the phase of iron oxide present in the plume depends on the oxygen pressure and temperature in the chamber and since originally it was not certain which phase was most likely to occur, the survey included FeO (Wüstite), Fe_2O_3 (hemalite) and Fe_3O_4 (Magnetite). The results of this survey are summarized below.

All the iron oxides are darkly colored and strongly absorbing at room temperature in most of the visible region. That is, their electronic band absorption edge extends into the visible, in contrast to, say, Al_2O_3 . However, in the near IR and IR regions, they are relatively transparent. The absorption again increases in the region of the lattice vibrations (~ 17.5 to ~ 30.3 microns). Pure $\alpha\text{-Fe}_2\text{O}_3$ has a very low conductivity at room temperature¹⁴ ($\sim 10^{-18} \text{ ohm}^{-1} \text{ cm}^{-1}$), with an activation energy of the order of 1 eV. The conductivity increases to $5 \text{ ohm}^{-1} \text{ cm}^{-1}$ at 1310°C .¹⁵ Magnetite and Wüstite are much better conductors, with conductivities of the order of $300 \text{ ohm}^{-1} \text{ cm}^{-1}$ and $30 \text{ ohm}^{-1} \text{ cm}^{-1}$, respectively, at room temperature.¹⁵

Absorption spectra have been obtained by two methods, (1) thin-film-substrate transmission studies (polycrystalline films 10-15 μ thick), and (2) powdered oxides compressed in optical disks such as KBr. Extraction of the index of refraction n_1 and the absorption coefficient, n_2 , is complicated in case (1) by multiple reflections and interference, and in case (2), by the fact that the transmitted beam is also reduced by scattering. The absorption coefficient is similar to the attenuation coefficient, but not equal to it. Method (2) has been used to locate the lattice vibrations. Bailey¹⁶ has corrected the transmittance measurement of α -Fe₂O₃ for reflection, and plotted absorption coefficient, α , versus wave number in the region .59 to 1.0 micron. Morin¹⁷ gives % transmission in the same region for a film of 15 μ thickness, but does not mention corrections. No absorption measurements have been made in the 2.0 to 6.2 micron region except for Banks, et.al.¹⁸ who did not subtract out the quartz substrate transmission. This omission can be significant since quartz absorbs appreciably for $\lambda > 4 \mu$. Waldron¹⁹ reported the optical density (which we assume is $-\ln t$ or $-\log t$) of α -Fe₂O₃ powder in a KBr disk in the 6.7 to 33 micron region. McDevitt and Baun²⁰ and Vraty, et.al.²¹ report lattice vibrations band numbers for α -Fe₂O₃, γ -Fe₂O₃, and Fe₃O₄. No data were found for the absorption of FeO. The results of References 16, 17 and 19 are shown in Figure 2 on a log-log scale, which de-emphasizes the magnitude of the curve, but not the shape. The complex part of the index of refraction, $n_2 = \alpha\lambda/4\pi$ is also indicated. Lewis and Westwood²² obtained a value of $\alpha = 2.8 \times 10^5 \text{ cm}^{-1}$ and of $n_2 = 1.17$ at 0.526 micron. Holland²³ quotes $n_1 - n_2i = 3.46 - 1.07i$ at 0.546 micron.

The handbooks list a single value for n for each of the iron oxides. These are given below in Table 1. The literature did not provide any additional data, except for Lewis and Westwood.²² The average value of n_1 reported for a polycrystalline film of Fe₂O₃ was 3.1 in the spectral range 0.747 to 1.11 microns, which is consistent with the handbook value. The dispersion curve is closely related to the absorption curve. Since there are no very strong absorption peaks in the 1-2 μ region, it is

reasonable to use the quoted values in the IR also. The relative dielectric constants of FeO and Fe₂O₃ are 12.7 and 12, respectively, supporting the assumption of similar indices of refraction. Also, in the case of α -Fe₂O₃, since the conductivity is so low, the static limit of $n_1 = (\epsilon)^{1/2} = 3.5$ is not a marked increase over the value in the near IR.

TABLE 1
REAL PART OF THE INDEX OF REFRACTION OF IRON OXIDES^(24,25)

<u>Oxide</u>	<u>n_1</u>	<u>$\lambda(\mu)$</u>
Fe ₂ O ₃ Hematite	$n_o = 3.220, n_e = 2.940$	0.6708
Fe ₃ O ₄ Magnetite	$n_1 = 2.42$ (average) $2.41 < n_1 < 2.46$	0.439 to 0.704
FeO	$n_1 = 2.32$	

All of the above data were obtained essentially at room temperature. In the absence of data at higher temperatures, and of more specific information on the spectral dependence of refractive index, ferric oxide was neglected in the present calculations. However, the available refractive index data indicates that Fe₂O₃ may be a significant IR emitter. This subject is discussed further in Paragraph 3.1.3.

Refractive index data for alumina, which is now considered as the sole continuum emitter in the plume, is shown in Table 2 and Figure 3. Bartky and Bauer²⁶ have tabulated best estimates of the real part of the refractive index, n_1 , for solid alumina. No data on n_1 exists for molten alumina. However since the variation of n_1 with temperature for solid Al₂O₃ is almost negligible, it is assumed that n_1 does not change when the alumina melts. The imaginary part of the refractive index, n_2 , for molten alumina is shown in Figure 3 which, for comparison, includes the data for solid Al₂O₃. For solid alumina, measurements²⁷ of n_2 have

TABLE 2
COMPLEX REFRACTIVE INDEX OF Al_2O_3 AS FUNCTIONS OF
WAVELENGTH AND TEMPERATURE

λ	n_1/n_2^a				
	1200°C	1500°C	1600°C	1700°C	2020°C
0.5	1.805/1.8-7	1.814/5.2-7	1.817/1.1-6	1.82/1.6-6	1.83/1.2-6
1	1.785/6.8-8	1.794/4.4-7	1.797/1.2-6	1.80/1.8-6	1.81/1.6-6
2	1.775/5.3-8	1.784/3.8-7	1.787/1.0-6	1.79/1.9-6	1.80/2.2-6
3	1.745/1.9-7	1.754/8.4-7	1.757/1.7-6	1.76/2.4-6	1.77/3.6-6
4	1.715/1.4-5	1.724/2.0-5	1.727/2.4-5	1.73/2.9-5	1.74/3.5-5
5	1.665/1.6-4	1.674/2.3-4	1.677/(2.8-4)	1.68/(3.2-4)	1.69/3.7-4
6	1.574/(9.1-4)	1.584/(1.1-3)	1.587/(1.4-3)	1.59/(1.6-3)	1.60/1.9-3

^aThe value of n_1 is given before the virgule; the value of n_2 is given after.

The - sign in n_2 indicates a negative power of ten. Thus 1.8-7 means 1.8×10^{-7} .

Parentheses denote values obtained by extrapolation.

been made over the wavelength interval from 0.5 to 6 μ , for temperatures from 1473°K to 2320°K. For molten alumina, measurements are limited to the interval from 1 to 2.5 μ ,¹⁰ although data have also been obtained by several investigators^{10,28} at 0.5 μ . Beyond 2.5 μ , the liquid n_2 curves were extrapolated arbitrarily, as shown in Figure 3. The consequences of this extrapolation are discussed later.

2.2.3 CLOUD OPTICAL PROPERTIES

A particle cloud such as a two phase rocket plume generally contains many particles of different size and often, of different kinds.

Within a small volume, we write for each particle,

$$I_i = F_i(\theta, \phi) / k^2 R^2 \quad (2-13)$$

so that the total scattered intensity is obtained by summation:

$$I = \sum_i I_i \quad (2-14)$$

and

$$F(\theta, \phi) = \sum_i F_i(\theta, \phi) \quad (2-15)$$

For the scalar sum indicated here, it is required only that there be no systematic relation between the phases of the light scattered by the different particles for $\theta \neq 0$. Due to the random momentary positions of the particles in the medium, their wide spacings relative to their size, and to the fluctuations on the phases of the light itself, the conditions for independent scattering are almost always met in a typical plume. Van de Hulst¹¹ mentions that early estimates indicate that the particles should be 3 or more radii apart for independent scattering. For particles of 1μ radius, typical of exhaust particles, this implies a concentration $\gtrsim 10^{10}$ particles/cm³ before the effects of dependent scattering become important. The SII ullage rocket considered in this report has a particle concentration of about 10^5 /cm³ at the nozzle exit.

The number distribution of particles in the plume is a function of position since the particle trajectories depends on particle size. Consequently the average absorption and scattering cross sections also depend on the position within the plume. The methods for determining the local average cross sections are described in the next paragraph.

2.3 PARTICLE PLUME PROPERTIES

2.3.1 LOCAL PARTICLE SIZE DISTRIBUTION

Computer Program B is used for the computation of the number density, particle size distribution, average radiative cross sections and particle energy fluxes at prescribed locations within the plume. These

locations are determined by input quantities specifying the number of equally spaced axial and radial locations desired. In addition, the particle trajectory program output is used to describe the limiting streamline and centerline properties of the various particle sizes in the plume. For simplicity the smallest particle size read-in is assumed to be the particle-plume boundary. In the cases reported herein this particle size was one-tenth micron. In addition, the particle size distribution is truncated along the centerline at the value of the maximum particle radius read-in which, for the case reported, was 20 microns. These arbitrary limits to the particle size distribution do not reduce the particle mass significantly, and, since actual knowledge of the extent of the distribution wings is highly debatable, the loss of accuracy here is not significant.

In order to determine the size distribution at an appropriate point, x, y , in the plume, the values of the limiting streamline and centerline properties are determined for each particle size at the axial location, x , prescribed. This is done by linear interpolation along the centerline and limiting streamline trajectories for the various quantities using x as the independent variable. The maximum particle radius is then determined at the particular value of y by interpolating on the limiting streamline values of y as a function of particle radius to obtain the particle radius whose limiting streamline would go through the given point. This radius is then taken as the maximum since any larger particles would have a y value for the limiting streamline that would be smaller than this y and thus, the particle could not reach this radial position. A particle size interval is then set up by dividing this maximum particle radius by a prescribed number of intervals which is dependent upon the form of the initial particle size distribution. Generally 50 intervals is satisfactory. The values of the particle radius in this new array will be designated as r'_p to distinguish them from the input array of r_p .

If one writes a particle continuity equation between the chamber and the prescribed x location in the plume, the following equation is obtained for a given size, r_p :

$$\frac{\rho_{p_x}}{\rho_{p_o}} = \frac{v_{p_{L_o}} + v_{p_{o_x}}^2 y_{p_{L_o}}^2}{\left(\frac{v_{p_{L_x}}}{2} + v_{p_{o_x}}\right) y_{p_{L_x}}^2} \quad (2-16)$$

where the particle velocity in the plume is assumed to be the average value between the limiting streamline value and the centerline value. From this expression one can compute the number of particles of a given size which are present at the plume location knowing the number which were present in the chamber and assuming that the particles of that size are equally distributed in both places. In this way the number density of each r'_p value is determined from the initial chamber size distribution and the interpolated value of the density ratio as given above.

This number density, computed for each r'_p value, constitutes a numerical size distribution at the plume position. The total number of particles is obtained by Simpson's integration over the individual r'_p array of number densities. A particle temperature is also computed at the appropriate value of x and y for each of the r'_p array by linearly interpolating with y between the limiting streamline and the centerline for the appropriate value of particle radius. The particle temperature for the r'_p array is then computed by interpolating on the r'_p array using r_p as the independent variable.

For the work reported here the initial size distribution in the chamber is given by the skew-symmetric formula of Bauer and Carlson:²⁹

$$\phi(r_p) = \frac{a^{b+1}}{b!} r_p^b e^{-ar} \quad (2-17)$$

where a and b are constants characterizing the distribution. For motors typical of the SII ullage $a = 1.78$ and $b = 1.0$, and r_p is in microns. Thus the mass mean diameter, d_{30} , is 3.24 microns while the number mean is 1.12 microns. The size distribution is shown graphically in Figure 4.

2.3.2 RADIATION PROPERTIES

The various average radiative properties are then computed at each plume position by the following equations:

$$\langle \sigma \rangle = \int_0^{r_{p_{\max}}} \frac{N(r_p) \sigma(r_p) dr_p}{N_t} \quad (2-18)$$

$$\langle \beta \rangle = \int_0^{r_{p_{\max}}} \frac{N(r_p) \beta(r_p) dr_p}{N_t} \quad (2-19)$$

$$B(T_{\text{eff}}) = \frac{1}{\langle \sigma_a \rangle} \int_0^{r_{p_{\max}}} \frac{N(r_p) \sigma_a(r_p) B(T(r_p)) dr_p}{N_t} \quad (2-20)$$

where $B(T)$ is the Planck blackbody function. The number density, $N(r_p)$, and the temperature, $T(r_p)$, are given by the particle trajectory program. The individual optical parameters for a given particle radius, temperature, and wavelength are obtained by linear interpolation from the tape, described in Paragraph 2.2.1, which summarizes the results of Mie theory calculations.

This completes the evaluation of the average local radiative properties at the various plume positions which are used in the calculation of radiation heating.

2.3.3 IMPINGEMENT PROPERTIES

The thermal and kinetic energy fluxes of the particles, which are required in order to evaluate particle impingement effects, are computed from the particle trajectory data by the following set of equations:

$$\text{K.E.} = \frac{2\pi\rho}{3} \int_0^{r_{p_{\max}}} r_p^3 v_p^3 N(r_p) dr_p \quad (2-21)$$

$$\text{T.E.} = \frac{4\pi\rho c}{3} \int_0^{r_{p_{\max}}} r_p^3 v_p T_p N(r_p) dr_p \quad (2-22)$$

Again the integrands are computed in the r'_p array and the total integration obtained by Simpson's method.

2.4 PARTICLE PLUME RADIATION

2.4.1 RADIATIVE TRANSFER IN A SCATTERING, ABSORBING, AND EMITTING MEDIUM

The discussion in the previous sections was concerned with calculating the scattering and absorption properties of individual particles and of the average properties of particles contained in an elemental volume of the plume large enough to contain many particles, but small enough that multiple scattering does not occur. The effect of multiple scattering is not a part of Mie theory at all, but is correctly treated by the equations of radiative transfer. This analysis begins with the integro-differential equation of radiation transfer in order to understand (1) the necessity of the various averaged properties, (2) the simplified equations and their solution and (3) the limitations of the solution.

Considering the geometry shown in Figure 5, the equation of radiative transfer for a medium containing a single type of particle can be written as:³⁰

$$dI_{\lambda}(x, \mu, \theta)/\mu dx = -N(\sigma_a + \sigma_s)I_{\lambda} + N(\sigma_s/4\pi) \int_0^{2\pi} \int_{-1}^{-1} \gamma(\theta(\mu, \theta, \mu', \theta')) I_{\lambda}(x, \mu', \theta') d\mu' d\theta' + N\sigma_a B_{\lambda}(T) \quad (2-23)$$

where the cross sections σ_a and σ_s are implicit functions of r, λ , and T , N is the number of particles per unit volume, and $\gamma(\theta)$ is the angular scattering distribution function, with

$$\int_0^{2\pi} \int_0^{\pi} \gamma(\theta) \sin\theta d\theta d\phi = 4\pi \quad (2-24)$$

When the medium contains particles of many sizes and possibly several materials, Equation (2-23) is usually solved by first omitting the emission term. Then, after the absorption has been calculated, the emittance is obtained by application of Kirchoff's law, which is permissible as long as the medium is in local thermodynamic equilibrium (LTE) but not necessarily in radiative equilibrium.

If the medium contains particles of many sizes in two or more materials, the summation over the size and material distributions must be taken. Again writing I for the average intensity at given values of the parameters λ , x , μ , and ϕ we have:

$$\mu \frac{dI}{dx} = N \sum_i C_i \left\{ \int_0^\infty \Phi_i(r_p) [-(\sigma_{i,s}(r_p, T) + \sigma_{i,a}(r_p, T)) I + \sigma_{i,s} \int_0^{2\pi} \int_{-1}^1 \frac{\gamma I d\mu' d\phi'}{4} + \sigma_{i,a} B(t(r_p))] dr_p \right\} \quad (2-25)$$

where

$$\int_0^\infty \Phi(r_p) dr_p = 1 \quad (2-26)$$

and C_i is the number fraction of particles of each composition with $\sum C_i =$ unity. Denoting the averages by $\langle \rangle$ we obtain finally

$$\mu \frac{dI}{dx} = -N(\langle \sigma_a \rangle + \langle \sigma_s \rangle) I + N \langle \sigma_s \rangle \int_0^{2\pi} \int_{-1}^1 \frac{\gamma I d\mu' d\phi'}{4} + N \langle \sigma_a \rangle B(T_{\text{eff}}) \quad (2-27)$$

It should be noted that T_{eff} is not the average particle temperature but rather a particle temperature which is determined from the following considerations for a non-isothermal particle cloud with a known distribution of particle sizes. If we require that the radiation from a differential volume of particle cloud be given by the average absorption cross section times the Planck function at a given effective temperature, we arrive at the equation below in which the term on the right is the summation of the contribution to radiation of each of the particles within the differential volume. This equation then yields the definition of the effective temperature.

$$\langle \sigma_a \rangle B(T_{\text{eff}}) = \int_0^\infty \frac{N(r_p) \sigma_a(r_p) B(T(r_p))}{N_t} dr_p \quad (2-28)$$

where

$$\langle \sigma_a \rangle = \int_0^\infty \frac{N(r_p) \sigma_a(r_p) dr_p}{N_t} \quad (2-29)$$

The discussion in Reference 26 indicates that the emittance, absorption, reflectance, and transmission can be considered functions of μ but not θ in the case of an extended homogeneous finite slab and that a good approximation to the normal emittance, reflectance, or transmission or to the hemispherical emittance, reflectance, or transmission can be obtained by use of the one-dimensional beam approximation.³¹ Solution of this approximation has been given²⁶ and will not be detailed in this write-up.

2.4.2 ONE-DIMENSIONAL BEAM APPROXIMATION

With the one-dimensional beam approximation,³¹ $\cos \chi = \mu$ now has only two values, ± 1 , corresponding to radiation in the direction of increasing x ($I(\mu = +1) \rightarrow I^+$) and in the direction of decreasing x ($I(\mu = -1) \rightarrow I^-$). Equation (2-27) is now replaced by the coupled equations:

$$dI^+/dx = -N(\langle \sigma_a \rangle + \langle \sigma_s \rangle) I^+ + \beta N \langle \sigma_s \rangle I^- + N \langle \sigma_a \rangle B(T_{\text{eff}}) \quad (2-30a)$$

$$dI^-/dx = -N(\langle \sigma_a \rangle + \langle \sigma_s \rangle) I^- + \beta N \langle \sigma_s \rangle I^+ + N \langle \sigma_a \rangle B(T_{\text{eff}}) \quad (2-30b)$$

When the particle temperatures and distributions vary significantly along the line of sight, the plume is divided into segments along the line of sight. For each segment, solution of the equation of radiative transfer yields:

$$I_m^+(\tau) = \frac{A_m}{2k_m} e^{k_m \tau} (K_m - k_m) + \frac{C_m}{2k_m} e^{k_m \tau} (K_m + k_m) + B(T_{\text{eff}}) \quad (2-31a)$$

$$I_m^-(\tau) = \frac{A_m}{2k_m} e^{-K_m \tau} (K_m + k_m) + \frac{C_m}{2k_m} e^{-K_m \tau} (K_m - k_m) + B(T_{eff}) \quad (2-31b)$$

where

$$\tau = N_t (\langle \sigma_a \rangle + \langle \sigma_s \rangle) x$$

$$k = \langle \sigma_a \rangle / (\langle \sigma_a \rangle + \langle \sigma_s \rangle)$$

$$K = \{k[2(1 - k)\beta + k]\}^{1/2} \quad (2-32)$$

$$\tau_{m-1} \leq \tau \leq \tau_m$$

and subscript m denotes the mth slab and A_m and C_m are constant coefficients.

The boundary conditions at each interface are:

$$I_{m-1}^+(\tau_{m-1}) = I_m^+(\tau_{m-1}) \quad (2-33a)$$

$$I_{m-1}^-(\tau_{m-1}) = I_m^-(\tau_{m-1}) \quad (2-33b)$$

In addition, at the surfaces τ_o and τ_n , the following boundary conditions are specified:

$$I_o^+(\tau_o) = \epsilon_o B(T_o) + r_o I_o^-(\tau_o) \quad (2-34a)$$

$$I_n^-(\tau_n) = \epsilon_n B(T_n) + r_n I_n^+(\tau_n) \quad (2-34b)$$

where ϵ and r are intrinsic properties of the outside regions and T is the corresponding temperature. Thus for n segments there is a $2n \times 2n$ matrix equation to be solved for the coefficients of the segment which radiates to the detector. The slab geometry for narrow and wide view detectors is shown in Figure 6.

Computer Program C performs the calculation described above along a line of sight in 3 dimensions. The number of intervals N and their spacing are determined by imposing a criterion on the variation of $B(T_{eff})$ within each segment. The properties chosen for each slab are those for the mid-point. The accuracy of this approximation is maintained by

limiting the change in the blackbody radiation based on the local effective temperature over the slab thickness to an arbitrary percent of the maximum value. The value of $B(T_{\text{eff}})$ is chosen for control for the following reasons: The radiation from a collection of particles depends on σ_a , β , $B(T_{\text{eff}})$ and the optical depth, $\tau = N(\sigma_a + \sigma_s)x$. This radiation is at most directly proportional to σ_a and τ . The dependence on T_{eff} , however, is much stronger. For $\lambda = 2 \mu$, $B(T_{\text{eff}}) \sim T^p$ where $6 > p > 2.5$ for $600 < T < 3000$ ($^{\circ}\text{K}$). Also for plumes, the greatest changes in the properties other than temperature occur in regions where dT/dx is large. Thus the magnitude of $B(T_{\text{eff}})$ seems the best criterion for slab thickness.

In addition to calculating the line of sight radiation as given by Equations (2-31) to (2-34), the computer also calculates "upper and lower bounds" corresponding to the hypothetical cases where $\beta = 0$ and $\beta = 1$. The case $\beta = 0$ is equivalent to no scattering, so that the region in front of the detector has maximum emittance and zero reflectance; the case $\beta = 1$ is equivalent to the minimum (but not zero) emittance and maximum reflectance in the same situation. For a very thin medium, the three results are the same, while for a dense medium they diverge.

2.4.2 POWER TO THE DETECTOR

In general the power per unit area of the detector per unit frequency interval is given by

$$\frac{P_d}{A_d \Delta\lambda} = \frac{I \Omega_d}{\pi} \quad (2-35)$$

where I is the angular dependent emitted intensity, Ω_d is the solid angle viewed by the detector and A_d is the detector area. The above equation can be used directly for the narrow angle detector. Since the line of sight is in the $\mu = 1$ direction for the calculation, I is the resultant normal emission.

In the case of the wide angle detector immersed in the plume the intensity will have a marked angular variation with the field of view and we must use

$$\frac{P_d}{A_d \Delta \lambda} = \frac{1}{\pi} \int_{\mu_{\max}^*}^{\mu_{\max}^*} \int_{\emptyset_{\min}^*}^{\emptyset_{\max}^*} I(\mu^*, \emptyset^*) \cos \xi(\mu^*, \emptyset^*) d\mu^* d\emptyset^* \quad (2-36)$$

where ξ is the angle between the normal to the detector area and the line of sight. If the detector is on the plume axis Equation (2-36) is replaced by:

$$\frac{P_d}{A_d \Delta \lambda} = 2 \int_0^{\mu_{\max}^*} I(\mu^*) \cos \xi(\mu^*) d\mu^* \quad (2-37)$$

For the general case in which I is a function of both \emptyset^* and μ^* , the following method is used to allow the proper spatial integration. Consider the μ^* -plane one that contains the axis and the target point, and the \emptyset^* -planes those normal to the μ^* -plane through the target point. The line of intersection of the two planes then makes the angle μ^* with the axis. The angle \emptyset^* is then the angle between the line of intersection and a given line of sight in the μ^* , \emptyset^* direction (i.e., in the $\emptyset^*(\mu^*)$ plane). If one specifies a group of μ^* directions (from μ_{\min}^* to μ_{\max}^*) and various \emptyset^* directions for each μ^* , the line of sight radiation is computed for each case. The resulting power is then found numerically (by hand) from Equation 2-36.

2.5 GAS RADIATION

At the initiation of the program it was assumed that gas radiation would be negligible compared to the particle continuum. During the course of the program, however, it was found that, for the lightly loaded SII ullage motor, gas plume radiation contributed a significant portion of the total flux. Since the plume was optically thin, calculation of the gas radiation could be made by hand. The calculation was simplified by the fact that the experimental measurement used for comparison was made with a narrow view radiometer. Consequently at the measuring station the plume was

divided into concentric cylinders whose average pressure, temperature, and species concentrations were specified by the results of the gas flow field calculations described earlier. Applying appropriate scaling laws for thin clouds, experimental data³²⁻³⁶ on gas emissivities were used then to determine band emission from the following species: H_2O , CO_2 , CO and HCl .

The approximate composition of the SII ullage exhaust is shown in Table 3. Radial pressure and temperature profiles at the measuring station, 6 inches downstream of the exit plane, are shown in Figure 7, which indicates also the concentric cylindrical zones used to subdivide the plume. Table 4 lists the average properties of each zone, including the partial pressure of the significant emitters.

TABLE 3
APPROXIMATE COMPOSITION OF S-II ULLAGE EXHAUST

	<u>Wt. %</u>	<u>Mole Fraction</u>
H_2O	23.865	0.368
H_2	0.749	0.104
CO	11.638	0.116
CO_2	19.073	0.120
N_2	9.819	0.098
HCl	25.436	0.194
OH	0.001	0
CL	0.012	0
$Al_2O_3(s)$	7.558	---
$FeO(s)$	1.799	---
O	0.048	0
	<hr/>	<hr/>
	99.998	1.000

TABLE 4
AVERAGE PROPERTIES FOR ZONES USED IN GAS RADIATION CALCULATION

<u>Zone</u>	<u>P_T, psf</u>	<u>T, °K</u>	<u>P_{H₂O}, atm</u>	<u>P_{CO₂}, atm</u>
I	1295	1600	.225	.074
II	1230	1500	.214	.070
III	1130	1500	.197	.064
IV	955	1500	.166	.054
V	760	1400	.132	.043
VI	490	1300	.085	.028
VII	280	1200	.049	.016
VIII	165	1000	.029	.010

SECTION 3

RESULTS AND DISCUSSION

3.1 PLUME RADIATION

3.1.1 EXPERIMENTAL RESULTS

During firings of the SII ullage motor at AEDC and OAL several radiometer measurements were made which can be used as a basis for comparison with the theoretical calculations. At AEDC³⁷ a Hayes FF1, narrow view (8 millirad x 8 millirad at 20 feet) detector, located 6 inches downstream of the exit plane and 5 ft from the plume centerline, was used to measure total radiation. The detector response was flat to 15 microns.³⁸ The results of this test, Figure 8, indicate an average steady state flux of $18 \text{ BTU/ft}^2 \text{ sec}$, or $6.53 \text{ watts/cm}^2\text{-ster}$.

At OAL³⁹ several spectral measurements were made over the wavelength interval from 0.5 to 3 microns. Results of these tests, shown in Figure 9, indicate that (1) on the basis of the AEDC test result, over one half of the radiative flux occurs at wavelengths greater than 3 microns and (2) in the observed spectral interval (1.7 to 3 μ) the gas band radiation is approximately one third of the particle continuum.

3.1.2 COMPUTATION

Results of the theoretical calculation, Figure 9, show that the particle continuum has a strong peak at approximately 1.2μ (corresponding roughly to the 2300°K blackbody peak, where 2300°K is the melting point of alumina) and has a low intensity, broad tail at longer wavelengths which peaks at about 8μ . The calculated radiancy in the visible spectrum is 10 times greater than the OAL observation, while the integrated continuum radiancy in the interval from 1.7 to 3 microns is about 13% of the experimental observation (excluding the gas bands). In addition, within this interval, the calculated peak is shifted from the observed peak toward the visible. The total integrated continuum flux is 10.5% of the total radiation measured by the FF1 detector.

Calculation of gas radiation was made for the following bands; 1.38, 1.87, 2.7 and 6.3μ bands of H_2O and 2.7 and 4.3μ bands of CO_2 . The 4.5μ band of CO was neglected since its contribution to the total gas phase radiation was small.³⁵ The 3.5μ band of HCl was also neglected since calculations based on the work of Stull and Plass³⁶ indicated a very small contribution. The gas band results, which are in excellent agreement with those obtained using an MSFC gas radiation computer program,⁴⁰ represent 23% of the total measured radiation.

Results of the gas calculation, superposed on the particle continuum, are compared with the OAL observations in Figure 9. It is seen that the calculation exceeds the measurement in the 2.7 micron range, but falls short of the measurement at other wavelengths by as much as a factor of 3. The total calculated radiation over the wavelength interval of 1.7 to 3 microns is in satisfactory agreement with the measurement. The total calculated gas plus particle radiation over all wavelengths is found to be 33.5% of the measured value. Causes for this discrepancy are discussed below, and studies are suggested which will provide the missing information on radiative properties of solid propellant combustion products.

3.1.3 DISCUSSION

Although the magnitude of the integrated radiative flux computed for the SII ullage motor is only 33.5% of the measured value, the predicted spectral radiancy over the interval from 0.5 to 3 μ is in qualitative agreement with the OAL spectral measurements. Thus both the calculation and the measurement provides evidence that the particle continuum is not grey-body. The consequences of the grey-body assumption are shown also in Figure 9, where the particle radiation calculated using the method of Morizumi and Carpenter¹ has been plotted. Morizumi and Carpenter assume a constant particle emissivity of 0.25. In the case of the SII ullage motor their method, together with the gas contribution, predicts 110% of the total measured radiation. However, as seen in Figure 9, the Morizumi and Carpenter method fails to provide an adequate description of the spectral distribution, being in error by as much as an order of magnitude at some wavelengths. Furthermore their assumption of a constant particle emissivity of 0.25 is seen to be a very poor approximation to the radiative properties of Al_2O_3 . Similarly, the treatment of Fontenot,² which is a simplification of the method of Morizumi and Carpenter, is equally inappropriate, since optical properties obtained from soot laden flames are assigned to alumina particles.

In view of the many inputs to the computer program, the discrepancy between the calculated and total measured radiation, roughly a factor of 3, is not surprising. If the gas calculation is assumed correct, the maximum discrepancy in the particle continuum is approximately a factor of 8. In order to determine the cause of this discrepancy, a number of factors, including uncertainties in the particle optical properties, the presence of other continuum emitters, and non-thermal radiative mechanisms have been investigated. Each is discussed in detail below.

a. Particle Properties

(1) Optical Data

For the present case, particles greater than 6μ diameter, which corresponds to 38% of the particle mass, are liquid. Thus the particle radiation is dominated by the liquid particles. However, in contrast to the solid alumina properties, the optical data for liquid alumina, which is available only in the wavelength region below 3μ , is highly uncertain. There is considerable scatter in the data of Carlson¹⁰ (a factor of about 8 near the melting point) and the data of Adams and Colucci²⁸ at 0.5μ is about a factor of 7 greater than that of Carlson at wavelengths from 1.4 to 2.3μ . By using mean values, the uncertainty due to scatter is a factor of about 3. Furthermore, as described earlier, the extrapolation of liquid alumina data beyond 3μ was purely arbitrary. A less conservative extrapolation, where the liquid n_2 curves parallel those for the solid beyond 3μ , would increase the long wavelength radiation by 4 times. In this case the calculated particle continuum would be 40% of the total measured radiation, so that with the gas contribution included, 63% of the measured radiation is accounted for.

(2) Supercooling

The possibility of supercooling of the particles below their fusion point and existence of a larger particle size distribution than used here can be discussed together since the essential feature of each is that a larger mass fraction of the alumina remains liquid. The optical data^{10,27} indicate an increase in the absorptivity of alumina of about 100 fold when it melts (at 2μ). Since calculations performed indicate that the SII ullage plume is optically thin at this measuring station, the radiation transport equation can be integrated for a single, homogeneous slab to yield:

$$I_o = N_t \langle \sigma_a \rangle B(T_{eff}) \Delta z \quad (3-1)$$

The use of one homogeneous slab is also based on the computed results which show that a central, homogeneous core about 17 cm in diameter contributes essentially the entire radiative flux. It can be shown further that the number density of particles is given by:

$$N_t = \frac{\phi_p / \rho_s}{4/3 \pi \int_0^{\infty} \Phi(r_p) r_p^3 dr_p} \quad (3-2)$$

while the average absorption cross section is given by:

$$\langle \sigma_a \rangle = \pi \int_0^{\infty} \Phi(r_p) Q_a(r_p) r_p^2 dr_p \quad (3-3)$$

If one assumes that the refractive index of alumina is near unity (i.e., $n_1 - 1 \ll 1$ and $n_2 \ll 1$), the absorption efficiency is approximately:

$$Q_a = 2 \left[\frac{8\pi r_p n_2}{3\lambda} \right] \quad (3-4)$$

Introducing this into Equation (3-3) yields, at a given wavelength:

$$\langle \sigma_a \rangle = \frac{16\pi^2}{3\lambda} \int_0^{\infty} n_2(T) \Phi(r_p) r_p^3 dr_p \quad (3-5)$$

In Equation (3-5) it is assumed that the particle temperature is a function of the particle radius. For simplicity let $n_2(T) = n_{2s}$ for all particles which are solid and $n_2(T) = n_{2\ell}$ for all liquid particles so that Equation (3-5) becomes

$$\langle \sigma_a \rangle = \frac{16\pi^2 n_{2\ell}}{3\lambda} \int_{r_{p_{melt}}}^{\infty} \Phi(r_p) r_p^3 dr_p \left[1 + \frac{n_{2s}}{n_{2\ell}} \frac{\int_0^{r_{p_{melt}}} \Phi(r_p) r_p^3 dr_p}{\int_{r_{p_{melt}}}^{\infty} \Phi(r_p) r_p^3 dr_p} \right] \quad (3-6)$$

Substituting Equation (3-6) into (3-1) and setting the second term to zero (since $n_{2s}/n_{2\ell}$ is of the order of 10^{-2}) yields the following:

$$I \sim n_{2\ell} \frac{\int_{r_{p_{\text{melt}}}}^{\infty} \phi(r_p) r_p^3 dr_p}{\int_0^{\infty} \phi(r_p) r_p^3 dr_p} \quad (3-7)$$

It is clear from Equation (3-7) that the radiation for the thin case is proportional to the liquid alumina value of n_2 times the fraction of the particle mass that is liquid, i.e., the liquid phase radiation dominates for liquid mass fractions above about 10^{-2} .

Since about 38% of the alumina mass is liquid, if one allows supercooling of the particles below their fusion point or increases the size distribution so that a larger fraction of the mass is liquid, the radiation in the 0.5 to 3 μ region could increase by a factor of 2.5. Actually this is a slightly optimistic estimate since, because of supercooling, the temperature of the smaller particles would be somewhat less than the melting point. The resulting decrease in the blackbody function for these particles should be small, however, since the particles less than 3 μ radius have just solidified at the plume location corresponding to the position of the radiometer. Over the entire spectrum, the effect of supercooling increases the calculated particle continuum to 25% of the measured total radiation.

It should be pointed out that if the alternate liquid n_2 extrapolation (which parallels the solid n_2 curve beyond 3 μ) is used, the above increase cannot be realized beyond 5 μ , since the long wavelength radiation becomes blackbody limited. In this case, the effect of supercooling would increase the calculated particle continuum to 55% of the measured total radiation.

(3) Size Distribution

In addition to the increase in the mass fraction of liquid, a larger size distribution would also introduce (because of increased lag) more mass at temperatures greater than the melting point, so that there would be an increase in the average liquid absorptivity. An estimate of this effect indicates that the particle radiation is approximately doubled by increasing the mass mean and number mean diameters to 6.2 and 1.50

microns respectively ($a = 0.8$, $b = 0.6$). Although this change in size is not unrealistic in view of existing particle size data, because of uncertainties in this data size effects were not further pursued.

b. Other Continuum Emitters

Investigation of other possible sources of continuum radiation has uncovered a very important factor, not previously recognized. The SII ullage motor contains almost 2 percent ferric oxide as a burning rate enhancer which should be condensed in the exhaust plume. In the present calculation this material was neglected since appropriate particle size data and optical data at elevated temperatures does not exist. However, the ferric oxide optical data that does exist, Figure 2, indicates that the value of n_2 for $\lambda = 1 \mu$ at room temperature is about 15 times the value for liquid alumina at its melting point and over 7 orders of magnitude larger than the room temperature value for alumina. If the value of n_2 for ferric oxide increases with temperature as does the alumina value its importance is obvious.

The possibility of ferric oxide being the primary continuum radiator is qualitatively substantiated by the CAL tests⁴¹ which show the following results for the S-IB retro which contains 2 percent ferric oxide but no alumina and the SII ullage which has a like amount of ferric oxide but 8 percent alumina.

TABLE 5
COMPARISON RADIATION FROM S-II ULLAGE AND S-IB RETRO MOTORS

	<u>SIB Retro</u>	<u>SII Ullage</u>
P_e	61 psia	14.6 psia
$I_{\lambda=2\mu}$	0.14	0.025
$I_{\lambda=2\mu}/P_e$	2.33×10^{-3}	1.71×10^{-3}

As can be seen the radiation values, normalized by pressure,* are comparable. Since the dominant radiation is apparently continuum, the importance of Fe_2O_3 is evident. The significance of the ferric oxide radiation is that other burn rate controls could be used with a resulting decrease in the continuum radiation level.

In addition to the ferric oxide content one must not overlook the possibility of the non-equilibrium formation of carbon particles. The report³⁷ on the experimental measurements notes the presence, at the end of the test, of soot on a probe that was located in the plume. It is not known whether this carbon particulate matter is present only on start-up and/or shut down (which would not affect the experiment) or is present during the steady state burn. It was also noted that part of the ablative nozzle was lost during the test. This nozzle ablation could have possibly introduced solid carbon into the plume mixing region. Unfortunately the importance of carbon radiation cannot be quantitatively estimated, but the possibility of its contribution must be noted.

c. Non-Thermal Radiative Mechanisms

(1) Searchlight Effect

The magnitude of the searchlight effect was calculated by computing scattered and emitted flux from particles having the SII ullage motor size distribution described previously. The throat radiation scattered over all angles by a single particle in the measurement volume is

$$F'_{se} = B(T_{ch}) A_t \omega_{th} \tau_{th} Q_s \quad (3-8)$$

and the flux scattered, per steradian, in the direction of the detector is

$$F_{se} \equiv \bar{f} F'_{se} \quad (3-9)$$

The emitted energy per steradian is

$$F_{em} = \epsilon_p B(T_p) A_p \quad (3-10)$$

*Nozzle size and temperatures were essentially the same for both motors.

In Equation (3-8), it is assumed that the throat transmits blackbody radiation at the chamber temperature.

The calculations were made using size distributions and particle temperature versus size as calculated by the computer program. Particle emissivity for the liquid was taken from Figure 3, except that beyond 3μ the liquid n_2 curves were extrapolated parallel to the solid curves. For the solid, the absorption coefficient data of Gryvnak and Burch²⁷ was used. The quantity Q_s was taken as constant and equal to 2.

A series of polar scattering diagrams were plotted to obtain the average 90° scattered energy into one steradian; Figures 10 and 11 are examples. Figure 12 shows the result plotted as a function of $2\pi r/\lambda$. The quantity \bar{f} can be seen to oscillate widely as particle size increases. The bar is to denote the fact that this scattered radiation is averaged over view angle for 2 reasons; first, the radiation scattered into one steradian, at 90° , is a strong function of the exact direction of look, and second, the particles viewed within the observed volume have scattering angles which deviate from 90° by angles ranging from zero to the nozzle half angle.

There is a strong scattering lobe at 70° in the forward direction for most particle sizes, and an intensity measurement made at angles centered about that value rather than 90° ought to favor searchlight emission - i.e., \bar{f} will be considerably larger on the average.

The ratio of scattered light (searchlight effect) to thermally emitted radiation is shown in Figure 13. Between 1.25 and 3.75μ and at wavelengths less than 0.75μ , the searchlight radiation dominates the thermal emission by amounts ranging up to a factor of nearly six. The thermal emission dominates either where the Planck spectrum (at the exhaust temperature) peaks, $\sim 1 \mu$, or where the particle emissivity becomes large ($\lambda \gtrsim 4 \mu$).

For the particular n_2 extrapolation used, searchlight emission increases the calculated particle continuum to 49% of the measured total radiation. If both supercooling and searchlight emission are included,

63% of the measured radiative flux can be attributed to the particles. Finally, by adding the gas contribution, the theoretical calculation accounts for 86% of the measured radiation.

Based on this hand calculation, it is concluded that for the case of the Saturn S-II ullage motor, the searchlight effect plays an important role in the spectral distribution of radiation, and may contribute significantly to the total radiant heat transfer. However, this conclusion should be accepted with the reservations that it is based on a rough hand calculation and that rather broad assumptions were made in computing the average flux scattered into one steradian centered at 90° .

(2) Non-Equilibrium Gas Radiation

In computing gas and particle radiation, it has been assumed that the gas is in complete thermodynamic equilibrium. However, it is known that non-equilibrium effects begin to dominate the thermochemical gas properties, beginning at a nozzle expansion area ratio of about 2 to 4, just downstream of the throat.⁴² In this paragraph the possibility that non-equilibrium processes may enhance the (equilibrium) gas radiation is explored briefly.

The following three physical effects may contribute to this radiation: (1) the recombination of two species to form a single molecular product may release the excess (binding) energy in the form of continuum radiation; (2) the excited vibrational levels of H_2O and CO_2 may lag the rapid decrease of gas temperature in the nozzle expansion, leading to non-equilibrium radiation which exceeds the equilibrium value; (3) the excited vibrational levels of H_2O and CO_2 may be fed by 3-body collisional recombination of atoms and free radicals, producing non-equilibrium radiation in excess of the equilibrium value. Each of these three non-equilibrium radiative processes is evaluated semi-quantitatively below, for the conditions of the SII ullage plume radiation measurement 6 inches downstream of the exit plane.

The power emitted per unit volume by two-body radiative recombination processes of the type $A + B \rightarrow AB + h\nu$ is

$$w = Ah\nu k_1 X_A X_B (\rho/M)^2 \quad (3-11)$$

The mole fractions, X_A and X_B , of recombining atoms at the point of measurement are determined by the non-equilibrium nozzle expansion process discussed in Reference 42. There it is shown that a single freezing point occurs in the nozzle expansion. Upstream of this point the recombining species remain nearly in equilibrium; downstream of this point the sum of the mole fractions of the recombining species remains nearly constant (frozen) at the freezing point value. The freezing point, denoted by starred quantities, is located by equating the total available three-body recombination rate to the required total equilibrium rate of decrease of atomic and free radical species:

$$\sum_{i,j,m} k_{ijm} X_i X_j X_m \left(\frac{\rho}{M}\right)^3 = \frac{d(\sum_i X_i)}{dx} \left(\frac{\rho}{M}\right) v_g^* \quad (3-12)$$

The freezing point is usually found just downstream of the nozzle throat. For the SII ullage motor composition, the abundant atom and free radical species at an area ratio of 2.1, downstream of the throat, are Cl, H, and OH, with equilibrium mole fractions of .0018, .0011, and .00082, respectively. The most rapid k_{ijm} known to the authors is that for the reaction $H + OH + H_2O \rightarrow 2H_2O$, ($k = 1.6 \times 10^{17} \text{ cm}^6/\text{mole}^2\text{-sec}$)⁴² and will be used here as representative of the sum $\sum_{i,j,m} k_{ijm} X_i X_j X_m$. Rates for $H + Cl + M \rightarrow HCl + M$ or $OH + Cl + M \rightarrow HClO + M$ are not known, but are probably not faster. The Cl can be combined via the reaction $H + OH + H_2O \rightarrow 2H_2O$ plus the rapid transfer reaction $H_2O + Cl \rightarrow HCl + OH$.

Using the mole fractions and the derivatives found from the Aeronutronic free-energy-minimization equilibrium nozzle expansion computer program, the freezing point is found to be at an area ratio of 2.3, where $X_H^* = .00095$, and $(\rho/M)^* = 3.5 \times 10^{-5} \text{ moles/cm}^3$.

The information on radiative recombination rate processes and rate constants is extensive, but often not definitive. The rate constant for the process $O + NO \rightarrow NO_2 + h\nu$ has been studied extensively⁴³ and is $1.1 \times 10^{11} T^{-1.59} \exp(670/RT) \text{ cm}^3/\text{mole-sec}$ in the temperature range 200 to

4000°K. This particular process will not produce significant non-equilibrium radiation in the SII ullage plume because of the low concentrations of O and NO. However analogous processes may be significant. Such processes will be most significant if one of the abundant free radicals, H, Cl, or OH combines with one of the major species, HCl, CO, CO₂, H₂, or N₂. A likely possibility is $H + CO \rightarrow HCO + h\nu$ and is chosen here as representative of all such possibilities. If this reaction has a rate constant comparable to that for $O + NO \rightarrow NO_2 + h\nu$, the total emission at the plume centerline at the location of the transverse radiative measurement would be 4.9×10^{-4} watts/cm³ (assuming $h\nu = 1$ e.v.). Assuming this is emitted over a 30 cm path length, the resultant integrated intensity would be .0012 watts/cm²-ster, which is a factor of 5000 smaller than the measured total emission from the SII ullage motor.

For this non-equilibrium process to be significant in this case, a radiative recombination rate constant three orders of magnitude larger than that assumed above would be necessary. Such large rate constants have been suggested, but only for atom-atom recombination. Because the atom concentration is 100 times smaller than that of CO, used in the example above, the atom-atom process would not be significant, even with the higher rate. It is concluded that this class of non-equilibrium processes is probably not significant in producing plume radiation heating. However processes such as $H + Cl \rightarrow HCl + h\nu$ bear further evaluation if literature reports are found of rate constants five or more orders of magnitude larger than that for $O + NO \rightarrow NO_2 + h\nu$.

The second and third non-equilibrium processes involve discrete band emission, as compared to the continuum emission produced by the radiative recombination process described above. The second process is readily shown to be insignificant through a brief review of previously measured vibration relaxation times of CO₂ and H₂O. In Table 5.13, Cottrell and McCoubrey⁴⁴ give a collision number of 110 at a temperature of 1031°K for vibration relaxation of CO₂ by collisions with CO₂, and it is steadily decreasing with increasing temperature. In CO₂-N₂-He pulsed

laser measurements at room temperature, Weber and Deutsch⁴⁵ show the relaxation of the slowest vibration level of CO₂ (that responsible for the 4.3 μ band emission) due to He collisions near room temperature to vary as $t(\text{millisec}) = 2/p(\text{torr})$. H₂ is known to be even more effective than He in this respect. These two relaxation times are about the same for the conditions of the plume measurement, being 2×10^{-5} sec, considerably shorter than the characteristic time of 5×10^{-5} sec for the flow to cover a distance of 10 cm, typical of the scale length over which the gas changes temperature significantly.

Cottrell and McCoubrey⁴⁴ give comparable, or faster, relaxation rates for H₂O at temperatures approaching 1000°K. Since the collisional relaxation time varies inversely with gas density, regions upstream of the radiation measuring station are expected to be very close to vibrational equilibrium. Thus vibration excitation in the chamber is not retained through the nozzle expansion and emitted later in the plume.

The third possibility to produce non-equilibrium radiation is the feeding of recombination energy into the excited vibrational levels, thereby distorting the equilibrium thermal distribution. As shown previously, there is a freezing point beyond which the atom and free radical mole fractions remain much higher than the local, shifting equilibrium values. The maximum energy available for radiation emission is

$$W = Ah\nu_{i,j,m} \sum k_{ijm} X_i X_j X_m \left(\frac{\rho}{M}\right)^3 \quad (3-13)$$

Using the freezing point mole fractions for H, OH, and H₂O, $k = 1.6 \times 10^{17}$, quoted earlier, $h\nu = 5 \text{ e.v.}$, and (ρ/M) at the measuring station of 5.4×10^{-6} , W is 3.1 watts/cm^3 , or $7.4 \text{ watts/cm}^2\text{-ster}$ over a 30 cm path length. This is comparable with the measured radiation emission and bears further investigation.

The fraction of this energy that is actually radiated depends roughly on the ratio of the radiative decay rate to the collisional decay rate of the excited vibrational levels. For example, the radiative

lifetime of the 00^0_1 state of CO_2 , which is responsible for the 4.3μ radiation, is approximately 2.3 milliseconds, whereas the collisional relaxation time of this state is two orders of magnitude shorter. If this ratio is roughly correct for other states of CO_2 and H_2O , it would be expected that no more than 1% of the available recombination energy would be radiated; the remaining 99% would go into thermal energy of the gas. Thus this non-equilibrium radiation mechanism is also expected to be unimportant.

In summary, the three non-equilibrium radiation mechanisms known to the authors and studied semi-quantitatively here do not appear to be of sufficient magnitude to warrant more careful attention at this time.

d. Comparison with Other Spectra

It is also of interest to compare some other solid propellant spectra with the shape of the spectrum computed for the no supercooling case. Figures 14 and 15 show solid fueled booster spectra for flight and ground based measurements respectively. In Figure 14, the particle continuum in the 1 to 3μ wavelength region shows the same shape as the computed continuum, although the H_2O band centers are absorbed because of atmospheric transmission losses. The large peak at 4.8μ is also duplicated by the calculated peak but its width is much narrower. The experimental peak could be a wing of the 4.3μ CO_2 band, or it could actually be due to particle emission with the rapid drop-off at 5μ due to a decrease in detector sensitivity.

Figure 15 shows the same computed spectrum compared with the ground test of another aluminized booster. Again, a peak at 4.8μ is noted, but the short wavelength continuum is much stronger. It should be noted that this booster is considerably larger than the SII ullage motor. The water and CO_2 band centers are again absorbed after atmospheric transmission.

The spectra of Figures 14 and 15 do not provide any quantitative verification of the present model since thrusts, pressures, temperatures, and measurement geometries and techniques of the several motors are

different. However, they are presented to demonstrate the qualitative aspects of two-phase plume radiation over a wider wavelength region than was available for the SII ullage tests.

3.2 PARTICLE IMPINGEMENT EFFECTS

As stated earlier an important effect associated with the two phase exhaust from a solid propellant motor is impingement of the condensed phase particles on neighboring surfaces. During the impingement process a portion of the kinetic and thermal energy of the particles is transferred to the wall of the target causing removal of material. The effectiveness of this energy transfer process is commonly characterized in terms of an accommodation coefficient, α , which expresses the ratio of particle impingement heating to the energy content of the particle. While an accommodation coefficient can be defined for both the thermal and kinetic energy of the particle, inadequacies in available experimental data make such a differentiation difficult. Consequently it is common practice to define an overall accommodation factor based on the total particle energy.

In the following an analysis of particle impingement heating performed by the Boeing Co.,⁴⁶ based on test data obtained from an SII ullage firing, is reviewed with the purpose of (1) indicating areas of uncertainty, and (2) using the results of the plume program described earlier to refine the calculated values of α . In addition, several impingement tests performed at Aeronutronic using a helium-alumina particle-flow system and a Teflon model are described and accommodation factors corresponding to these conditions are reported and compared to the SII ullage results.

3.2.1 SII ULLAGE TESTS

An experimental investigation of heating from an SII ullage motor fired at sea level was performed by Rocketdyne.⁴⁷ This test program involved the mounting of a Teflon ablation probe and a copper heat transfer

probe 20 inches from the nozzle exit. The probes had a hemispherical nose 3 inches in diameter and were 5 inches long. The copper probe was instrumented to provide data on temperature distribution and stagnation point heat transfer. The ablation probe was instrumented to provide information on regression rate as well as stagnation point heating. In both cases the stagnation point heat transfer rate was approximately 3000 BTU/ft². In addition for the Teflon model a surface regression of 1.25 inches during a firing time of 3.6 seconds was reported.⁴⁸

Results of the Boeing analysis of the impingement heating data are shown in Table 6.⁴⁶ The radiant heating rate, q_R , was calculated using Fontenot's method.² The possibility of improving this calculation using the method developed here was considered unwarranted since in both instances q_R is of the order of 1% of the total measured heating rate. In Table 6 the convective heating rate, q_c , was evaluated using the Van Driest boundary layer theory for turbulent heat transfer to a blunt cone. The method of Fay and Riddell,⁴⁹ however, is considered to be more appropriate for calculating stagnation point heating, i.e.,

$$q_c = 0.76(Pr)^{-0.6}(\rho_w/\mu_w)^{0.1}(\rho_s\mu_s)^{0.4}(h_s - h_w)(dV_g/dx)_s^{0.5} \quad (3-14)$$

where, from modified Newtonian Flow theory, the stagnation point velocity gradient is given by:

$$(dV_g/dx)_s = [2(p_s - p_\infty)/\rho_s]^{1/2}/R \quad (3-15)$$

and Pr is the Prandtl number, ρ is the density, μ is the viscosity, h is the enthalpy, R is the radius of curvature at the stagnation point, p is the pressure and subscripts s , w , and ∞ denote shock, wall, and free-stream conditions, respectively. From the gas flow field computer program results described herein the SII ullage chamber pressure and temperature are 1000 psia and 6017°R respectively, while the gas molecular weight is 27.4 and the specific heat ratio is 1.21. From Reference 46, the center-line Mach number 20 inches downstream of the exit is 3.73 while the local

static pressure and temperature are 4.2 psia and 2485°R, respectively. Thus the post shock conditions can easily be calculated. In addition, for typical solid propellant exhaust gases:

$$\begin{aligned}\mu_w &= 1.75 \times 10^{-3} \text{ lb/ft sec} \\ \mu_s &= 6.4 \times 10^{-3} \text{ lb/ft sec} \\ C_{p_w} &= 0.40 \text{ BTU/lb}^\circ\text{F} \\ C_{p_s} &= 0.52 \text{ BTU/lb}^\circ\text{F}\end{aligned}$$

where the wall temperature is initially assumed to be 560°R. With the further assumption that $h = c_p T$, and $Pr = 0.85$, evaluation of Equation (3-14) yields:

$$q_c = 100 \text{ BTU/ft}^2 \text{ sec}$$

which is about 5 times less than the value listed in Table 6. It should be pointed out however that the gases evolved during ablation tend to thicken the stagnation boundary layer and that the heat transferred to the model will increase the model temperature. Since both factors diminish q_c , the value computed above represents a maximum convective heating rate. It is concluded, then, that the measured heating rate, q_{TME} , is due essentially to particle impingement.

A further improvement in the calculation of the accommodation factor is afforded by the particle plume structure results obtained from Program B. These computations were performed specifically for the SII ullage motor and should be more reliable than the assumptions used in the Boeing analysis. At a centerline location 20 inches downstream of the exit plane, the average particle thermal and kinetic energy fluxes determined by Program B were 4960 BTU/ft²sec and 6020 BTU/ft²sec respectively.* This corresponds to a total theoretical particle energy of 11980 BTU/ft²sec, approximately 21% greater than the value listed in Table 6. The difference

*In both the Boeing analysis and the present calculation, the contribution of ferric oxide is included. For this purpose it is assumed that the size distribution and thermal energy per unit mass of Fe₂O₃ is the same as for alumina.

TABLE 6
RESULTS OF ACCOMMODATION FACTOR STUDY⁴⁶

<u>Specimen Geometry</u>	<u>q_{TME}</u>	<u>q_R</u>	<u>q_c</u>	<u>q_{PEE}</u>	(1) <u>q_{TPE}</u>	(2) <u>q_{TPE}</u>	(1) <u>α</u>	(2) <u>α</u>
3" dia. hemi- spherical end of 5" long cyl.	3000	30	476	2494	9550	9896	0.261	0.252

All units in BTU/ft²sec

q_{TME} - total stagnation heating rate measured experimentally

q_R - theoretical radiant heating rate

q_c - theoretical convective heating rate

q_{PEE} - particle impingement heating rate = q_{TME} - q_R - q_c

q_{TPE} - sum of theoretical thermal and kinetic energy

α - accommodation coefficient = q_{PEE}/q_{TPE}

(1) - calculation based on uniform plume of 2 μ particles

(2) - calculation based on particle size distribution given in Reference 6.

is due primarily to an increase in the thermal energy flux, probably as a consequence of the more accurate determination of particle temperature that is possible using the appropriate flow field data. With these new values of q_{PEE} and q_{TPE}, α is 0.21.

3.2.2 AERONUTRONIC TESTS

Several particle impingement tests using a Teflon model in a helium-alumina particle stream were performed at Aeronutronic. A two phase flow was produced by injecting alumina particles, with a mass mean diameter of 4.46 μ, into a helium nozzle which exhausted into a vacuum

chamber. Teflon models, 1.0 inches in diameter x 1.0 inches long, were located coaxially on the nozzle centerline, 1.0 inches downstream from the exit plane. Tests were performed with helium stagnation temperatures of 540°R and 1000°R. Test data, together with theoretical values of particle thermal energy, q_{TTE} , and kinetic energy, q_{TKE} , are summarized in Table 7. Included also for comparison is similar information for the SII ullage motor.

Accommodation coefficients for the Aeronutronic tests can be determined with the help of a steady state ablation model. If the Teflon model is considered to ablate at a steady rate, an energy balance on the model yields:

$$q_{tot} = \dot{r}\rho[L + c\Delta T] \quad (3-16)$$

TABLE 7
SUMMARY OF AERONUTRONIC PARTICLE IMPINGEMENT TEST DATA

Test	v_p ft/sec	q_{TTE} BTU/ft ² sec	q_{TKE} BTU/ft ² sec	Surface Regression inches	Average Regression Rate-ft/sec	q_{TME} BTU/ft ² sec
Aero Cold He	4400	negl	256	.008	-	-
Aero Hot He	5800	negl	465	.009	-	-
SII ullage (Boeing)	6000	4960	6020	1.25	2.9×10^{-2}	3000

q_{TTE} - theoretical particle thermal energy flux

q_{TKE} - theoretical particle kinetic energy flux

where \dot{r} is the average regression rate, L is the heat of ablation of Teflon, $c\Delta T$ the increase in internal energy of the ablating element and:

$$q_{tot} = q_c + q_R + q_{PEE}$$

Since, for the Aeronutronic test conditions $q_{TTE} \approx 0$, then $q_{PEE} = \alpha q_{TKE}$ and if we further assume that $q_{PEE} \gg q_c + q_R$ then, after rearranging terms, we have:

$$\alpha = K\dot{r}/q_{TKE} \quad (3-17)$$

where $K = \rho[L + c\Delta T]$ is assumed constant for all conditions including the SII ullage firing. In fact, from the SII ullage data of Table 7, $K = 1.03 \times 10^5$ BTU/ft³.

The time to heat-up to the ablation temperature can be determined from the unsteady heat conduction equation for a semi-infinite slab:

$$T_x - T_\infty = \frac{2q_{tot}}{k} \left\{ \sqrt{\frac{\eta t}{\pi}} \exp\left(\frac{x^2}{4\eta t}\right) - \frac{x}{2} \operatorname{erfc}\left(\frac{x}{2\sqrt{\eta t}}\right) \right\} \quad (3-18)$$

where T is the temperature, k the thermal conductivity of Teflon, α the thermal diffusivity, x is the spatial coordinate normal to the surface, t is the time and subscript ∞ denotes the conditions at infinity. At the exposed surface, $x = 0$, the above equation reduces to:

$$t = \frac{\pi}{4\eta} \left(\frac{k(T_A - T_\infty)}{q_{tot}} \right)^2 \quad (3-19)$$

where T_A is the ablation temperature. For Teflon, typical thermal properties are:

$$k = .034 \text{ BTU/hr ft}^{20}\text{F/ft}$$

$$\eta = 3 \times 10^{-7} \text{ ft}^2/\text{sec}$$

Substituting these values into the above equation yields:

$$t = 3 \times 10^{-4} \left(\frac{\Delta T}{q_{tot}} \right)^2 \quad (3-20)$$

where t is in sec, q_{tot} is in BTU/ft²sec, and ΔT is in °F. The regression rate \dot{r} can be written as δ/θ where δ is the total surface regression, $\theta = t_t - t$, and t_t is the total test time. For the Aeronutronic tests, $t_t = 5$ sec. From Equation (3-16), since $K = \text{constant}$, we can write:

$$\left(\frac{q_{tot}}{\dot{r}}\right)_{\text{Aero}} = \left(\frac{q_{tot}}{\dot{r}}\right)_{\text{SII}}$$

Thus, q_{tot} for the Aeronutronic tests can be expressed as

$$q_{tot\text{Aero}} = \frac{\delta}{\theta} \left(\frac{q_{tot}}{\dot{r}}\right)_{\text{SII}}$$

or, substituting values from Table 7,

$$q_{tot\text{Aero}} = \frac{68}{5-t} \text{ BTU/ft}^2\text{sec} \quad (3-21a)$$

for the cold flow tests and

$$q_{tot\text{Aero}} = \frac{76}{5-t} \text{ BTU/ft}^2\text{sec} \quad (3-21b)$$

for the hot flow tests.

Combining this expression with Equation (3-20) and assuming that $\Delta T = 700^\circ\text{F}$, yields $t = 0.7$ sec. Assuming further that the transient from inception to steady ablation is negligible, the steady state ablation time is 4.3 sec. Finally, from Equation (3-17),

$$\alpha = .063$$

for the Aeronutronic cold test and

$$\alpha = .038$$

for the hot test.

At present there is no satisfactory explanation for the discrepancy between the results of the Aeronutronic tests and the SII ullage motor tests. Possible heat rejection mechanisms other than ablation (namely radiation emission from the model and convective cooling by the helium stream) have been examined and found to reject only a few percent of the heat input. The significant differences between the two

sets of data are (1) the free stream particle temperature, and (2) the total freestream energy flux. The lower particle temperature in the helium tests corresponds to higher yield strength and heat capacity of the particle which may lead to a more elastic particle-surface interaction, reducing the accommodation coefficient. The lower energy flux in the helium tests leads to a lower ablation rate and lower surface temperature, which may also influence the particle surface interaction processes and reduce the accommodation coefficient. Although the cold and hot helium tests do not follow these trends, the limited number of tests and the experimental uncertainties may be the source of the discrepancy. Further study of particle impingement damage is evidently needed.

SECTION 4

CONCLUSIONS AND RECOMMENDATIONS

On the basis of the preceding radiation calculations, it is not possible to isolate conclusively the physical mechanisms responsible for the plume emission. However, the following conclusions can be made.

Gas phase radiation clearly cannot be ignored, without demonstrating that its contribution is negligible. This is particularly true of lightly loaded solid propellant motors such as the SII ullage motor.

Insufficient alumina optical property data are available for valid predictions of alumina radiation at wavelengths less than 1.5μ and greater than 3μ . Furthermore, uncertainties in existing data are sufficient to account for a major fraction of the discrepancy between measurement and theoretical calculation.

While supercooling can explain 70% of the particle continuum, this requires a particular arbitrary extrapolation of the liquid alumina optical data. This mechanism is partially substantiated by the experimental spectrum ($1.7 - 3 \mu$) and partially refuted by it (visible region). Searchlight emission provides an alternative explanation of the observed radiation and the two effects combined account for 63% of the total experimental measurement.

Other solids, particularly iron oxide and possibly carbon cannot be dismissed as significant or even dominant contributors to particle radiation.

Additional experimental measurements of the SII ullage motor radiation at wavelengths greater than $4\ \mu$ would be invaluable in delineating and understanding the radiative mechanisms.

In view of the foregoing, the following areas of further study are recommended:

1. Extend the range of previous measurements of the emittance of liquid alumina particles to include the spectral regions from $.5$ to $1.5\ \mu$ and from 3 to $10\ \mu$.
2. Experimentally determine the optical properties of solid and liquid iron oxide particles over a spectral and temperature range appropriate for rocket exhaust plume radiation calculations.

This new data will not only provide for more accurate calculation of continuum radiation from solid propellant exhaust plumes, but should also permit a better evaluation of the significance of other major uncertainties, namely, particle supercooling and searchlight emission.

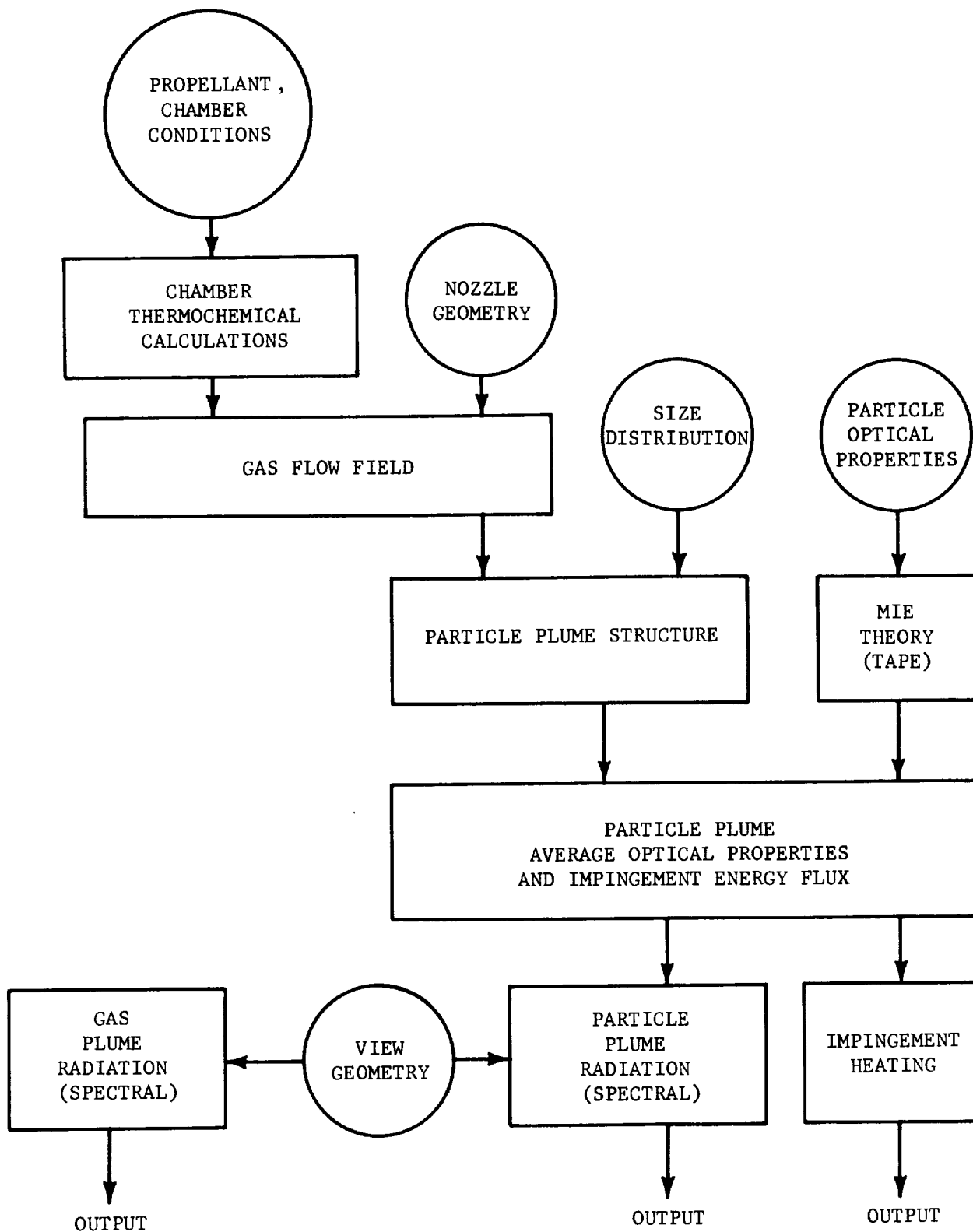


FIGURE 1. FLOW CHART OF CALCULATION SCHEME

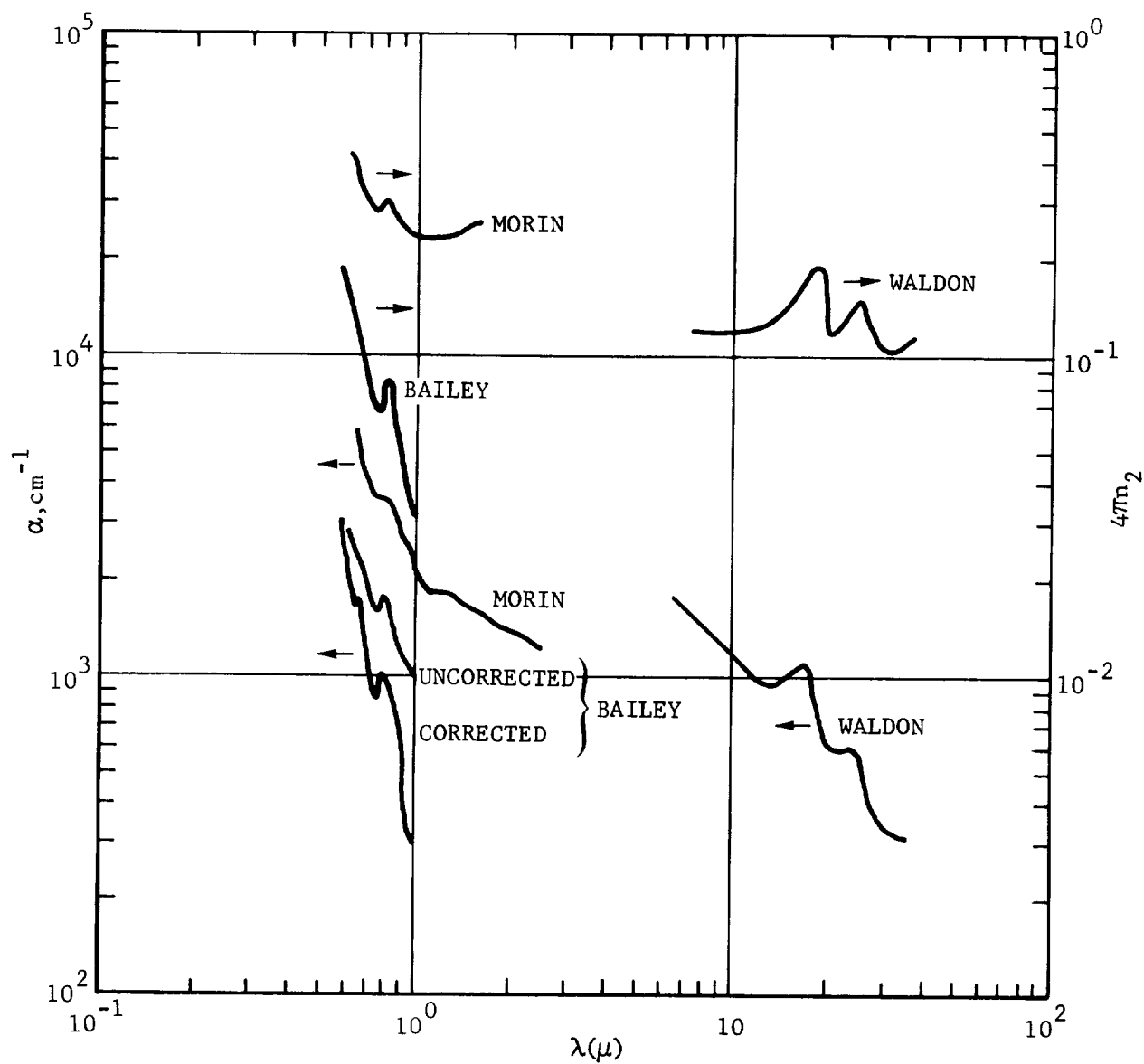


FIGURE 2. ABSORPTION COEFFICIENT AND INDEX OF REFRACTION OF $\alpha\text{-Fe}_2\text{O}_3$

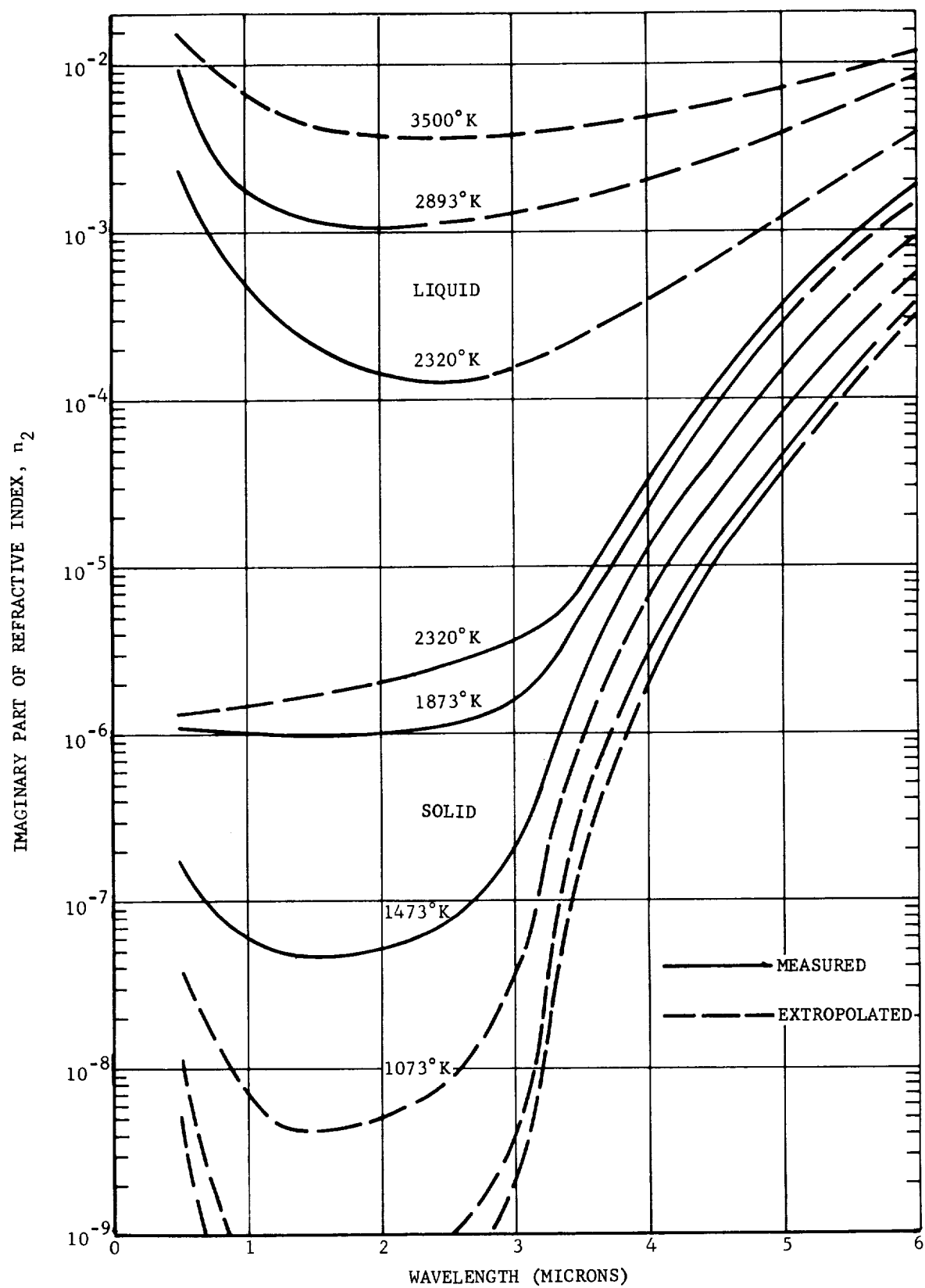


FIGURE 3. IMAGINARY PART OF REFRACTIVE INDEX OF ALUMINA

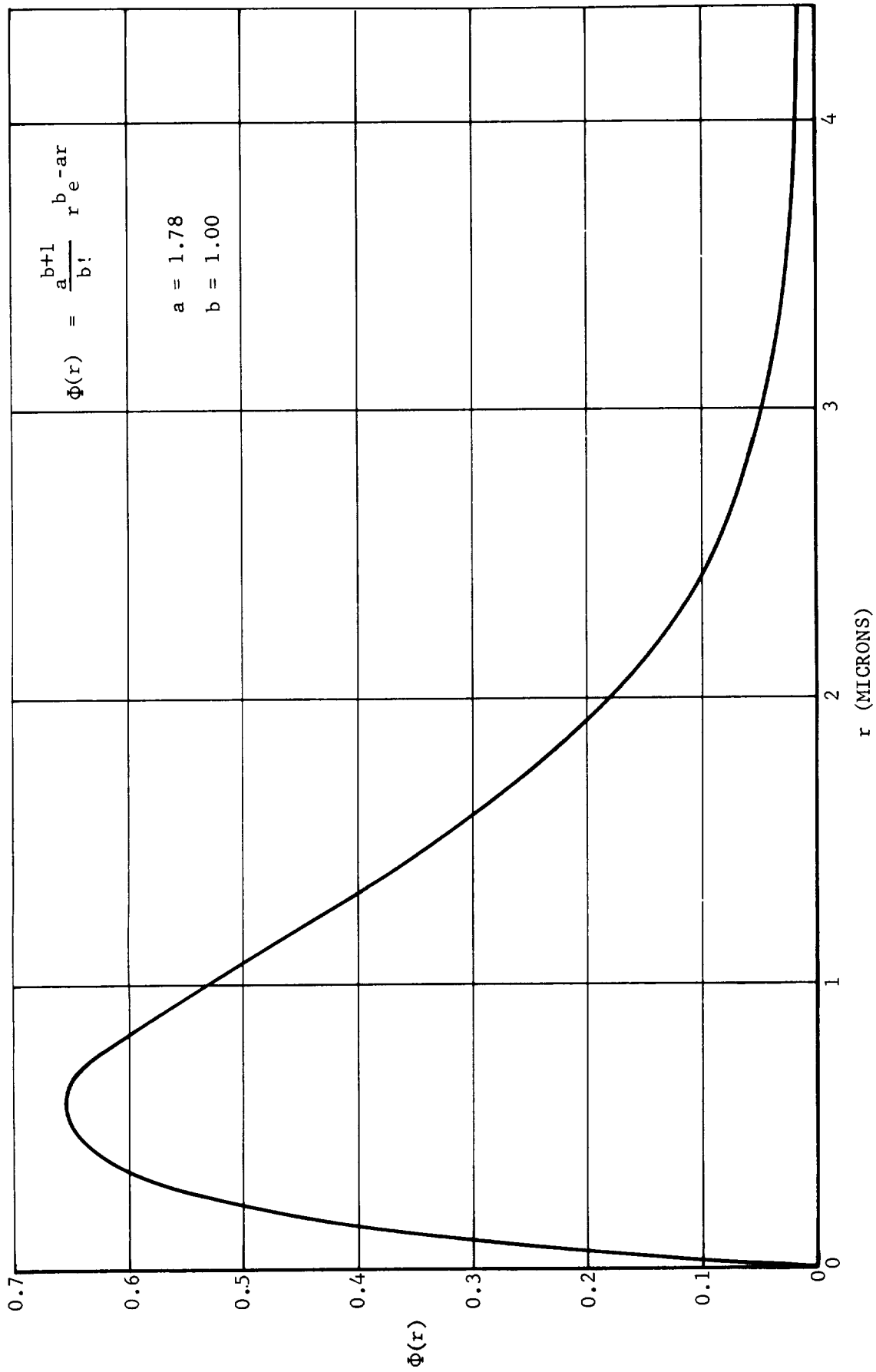


FIGURE 4. PARTICLE SIZE DISTRIBUTION FOR S11 ULLAGE MOTOR

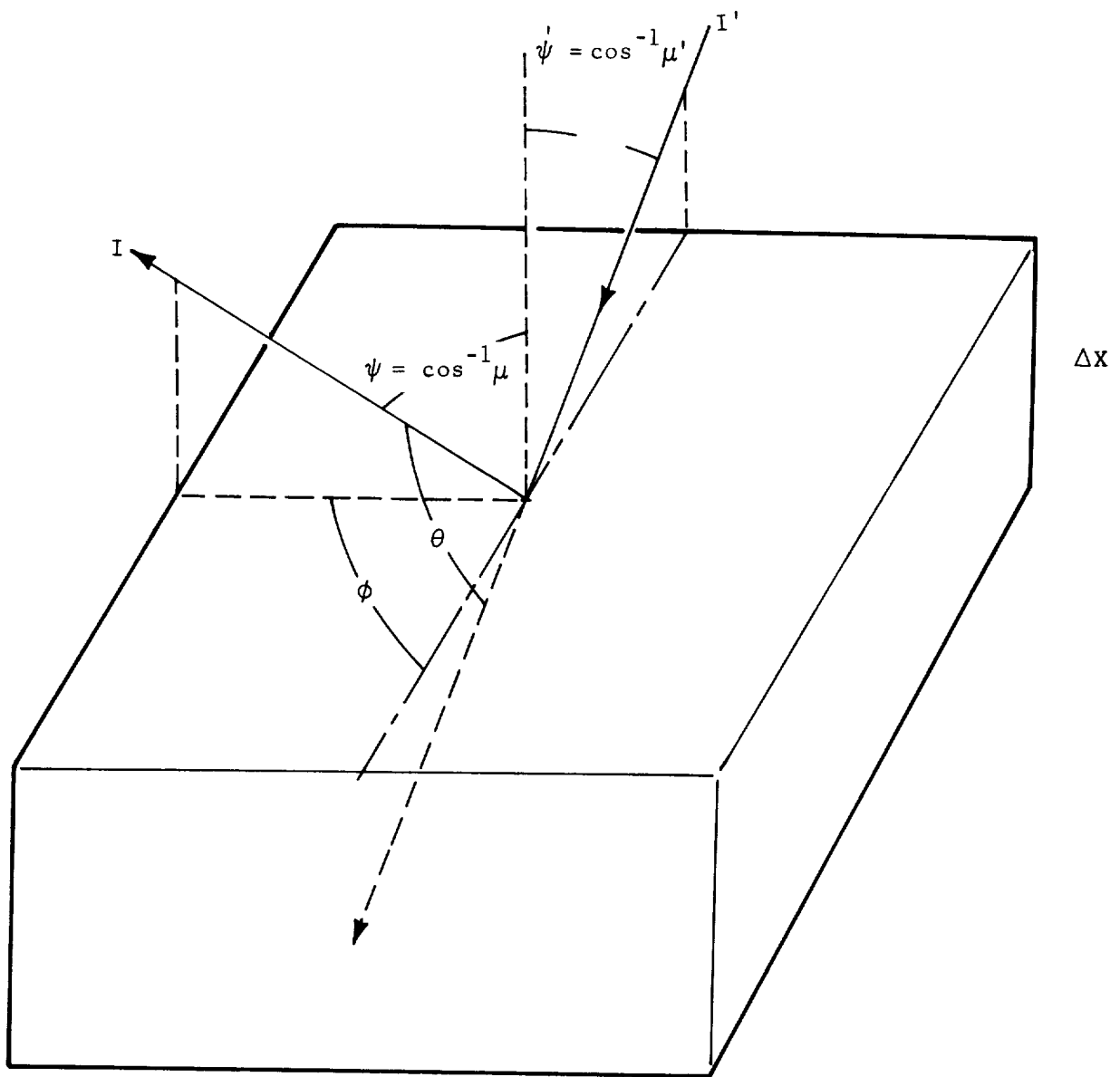


FIGURE 5. ILLUSTRATION OF COORDINATE SYSTEM FOR RADIATIVE TRANSFER PROBLEM

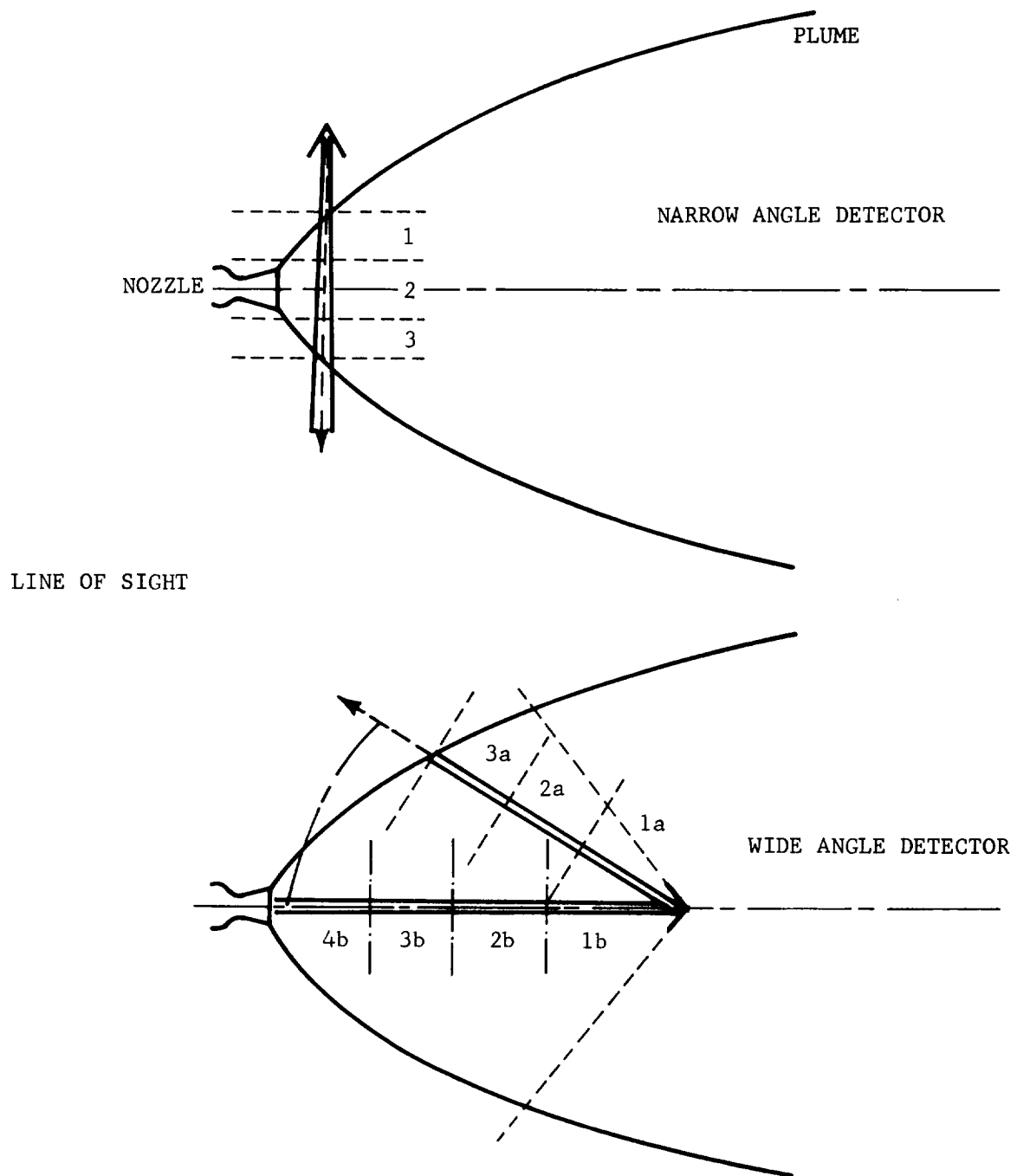


FIGURE 6. RADIATION DETECTOR VIEW GEOMETRY

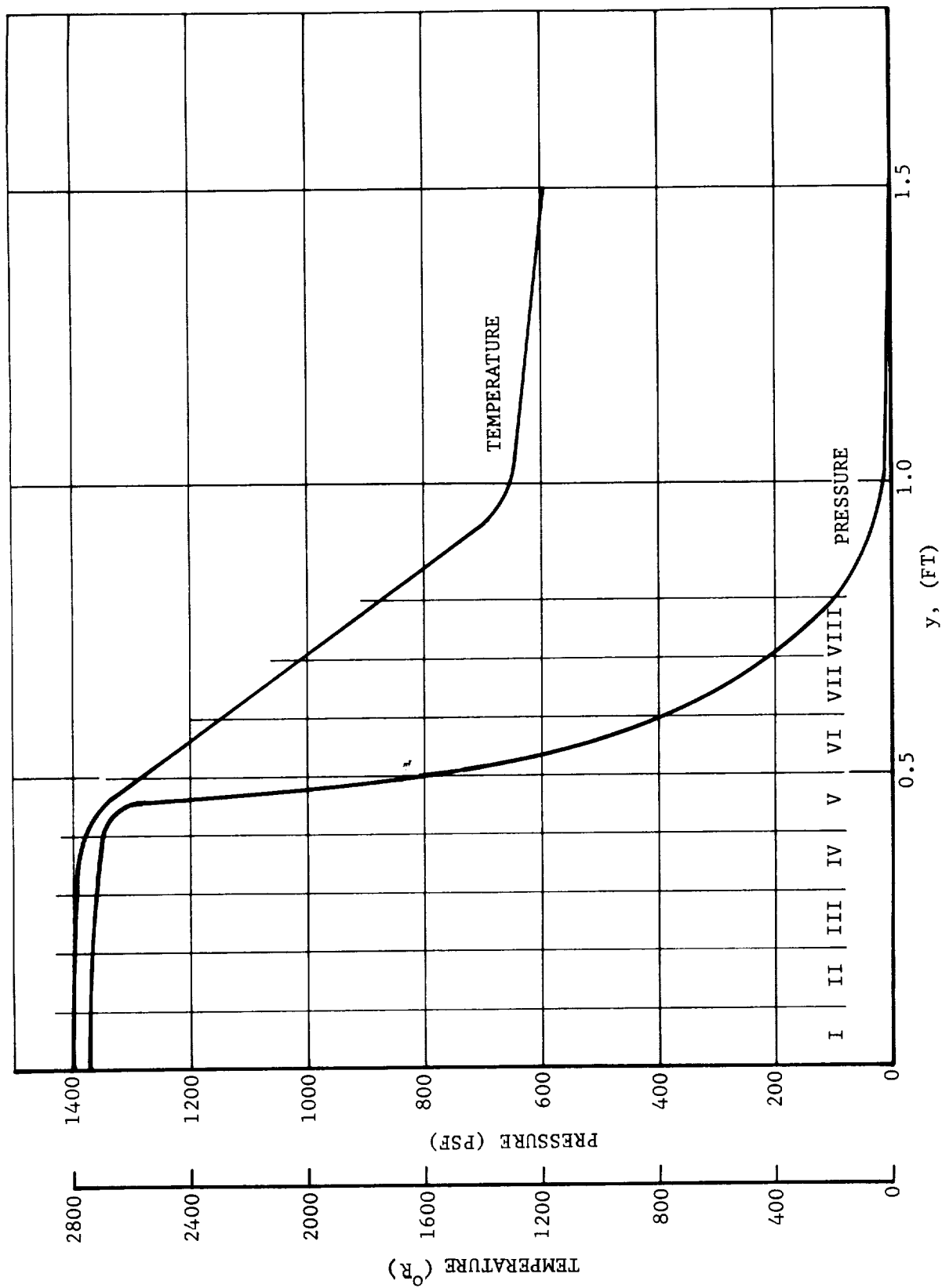


FIGURE 7. CALCULATED RADIAL PRESSURE AND TEMPERATURE PROFILE AT OBSERVATION STATION FOR S11 ULLAGE MOTOR PLUME

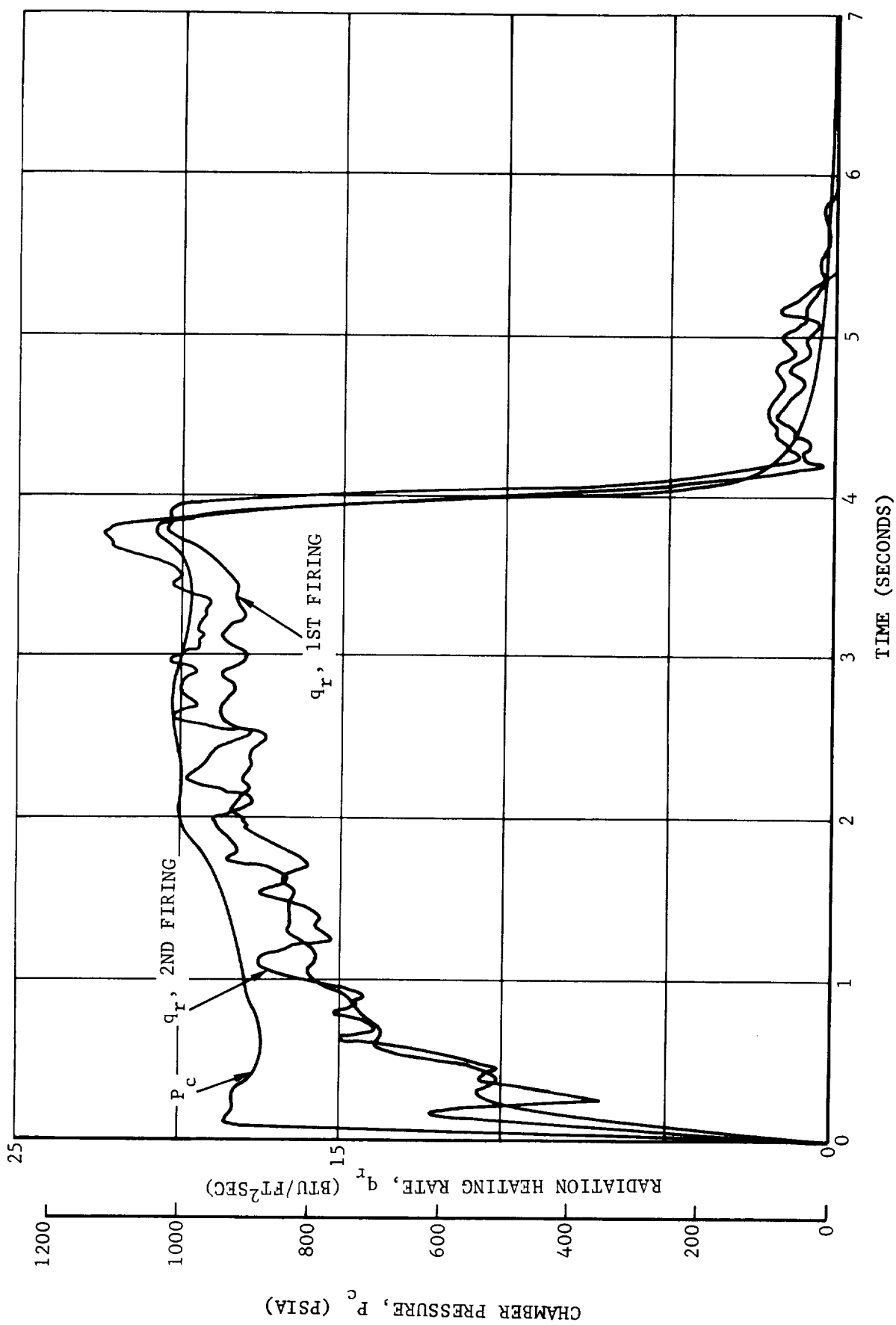
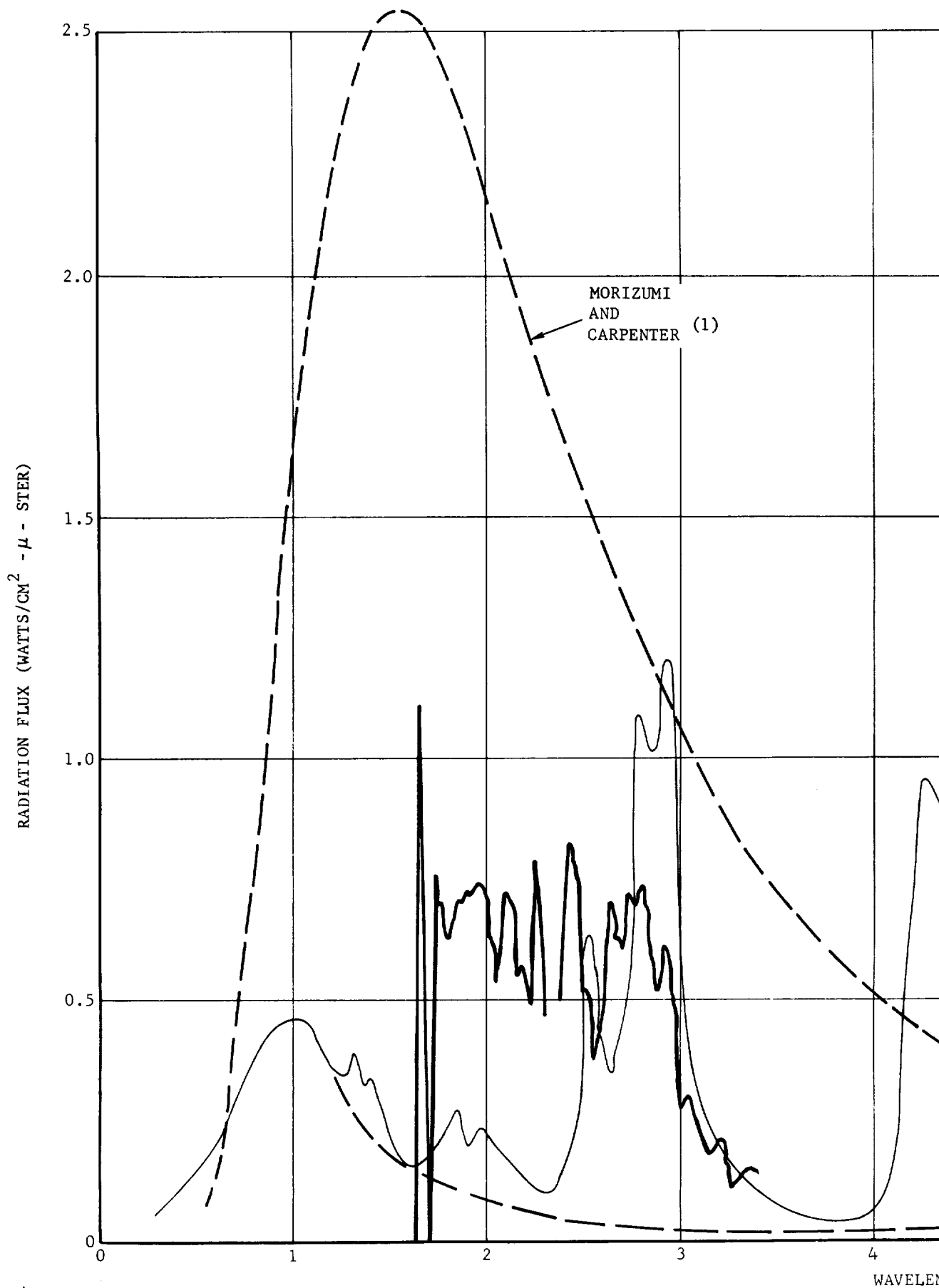


FIGURE 8. RADIATION HEATING RATES FOR S11 ULLAGE MOTOR 6 INCHES FROM EXIT PLANE USING MODEL FF-1 RADIOMETER

THIS PAGE INTENTIONALLY LEFT BLANK



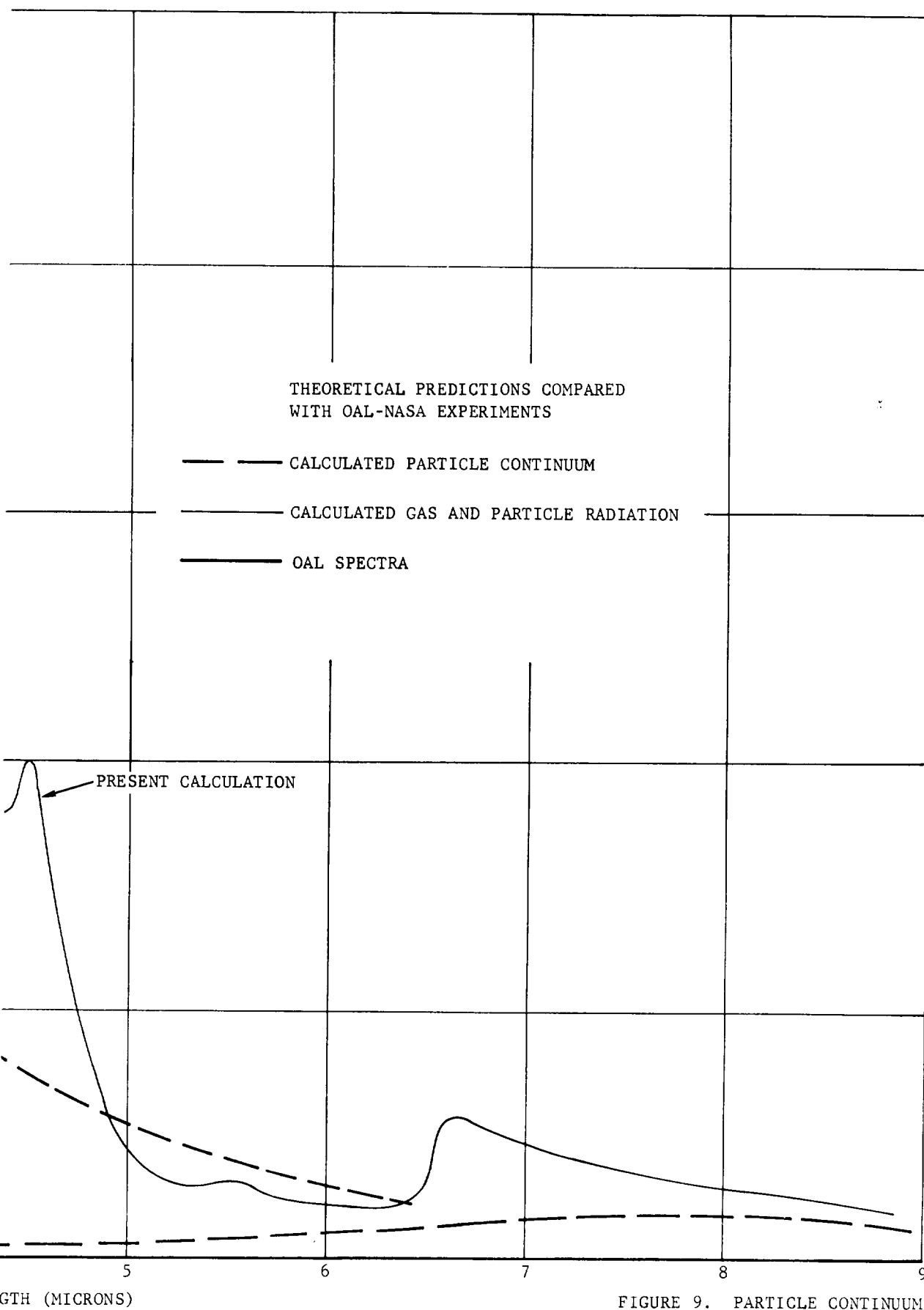


FIGURE 9. PARTICLE CONTINUUM AND GAS BAND
RADIATION FOR S11 ULLAGE MOTOR

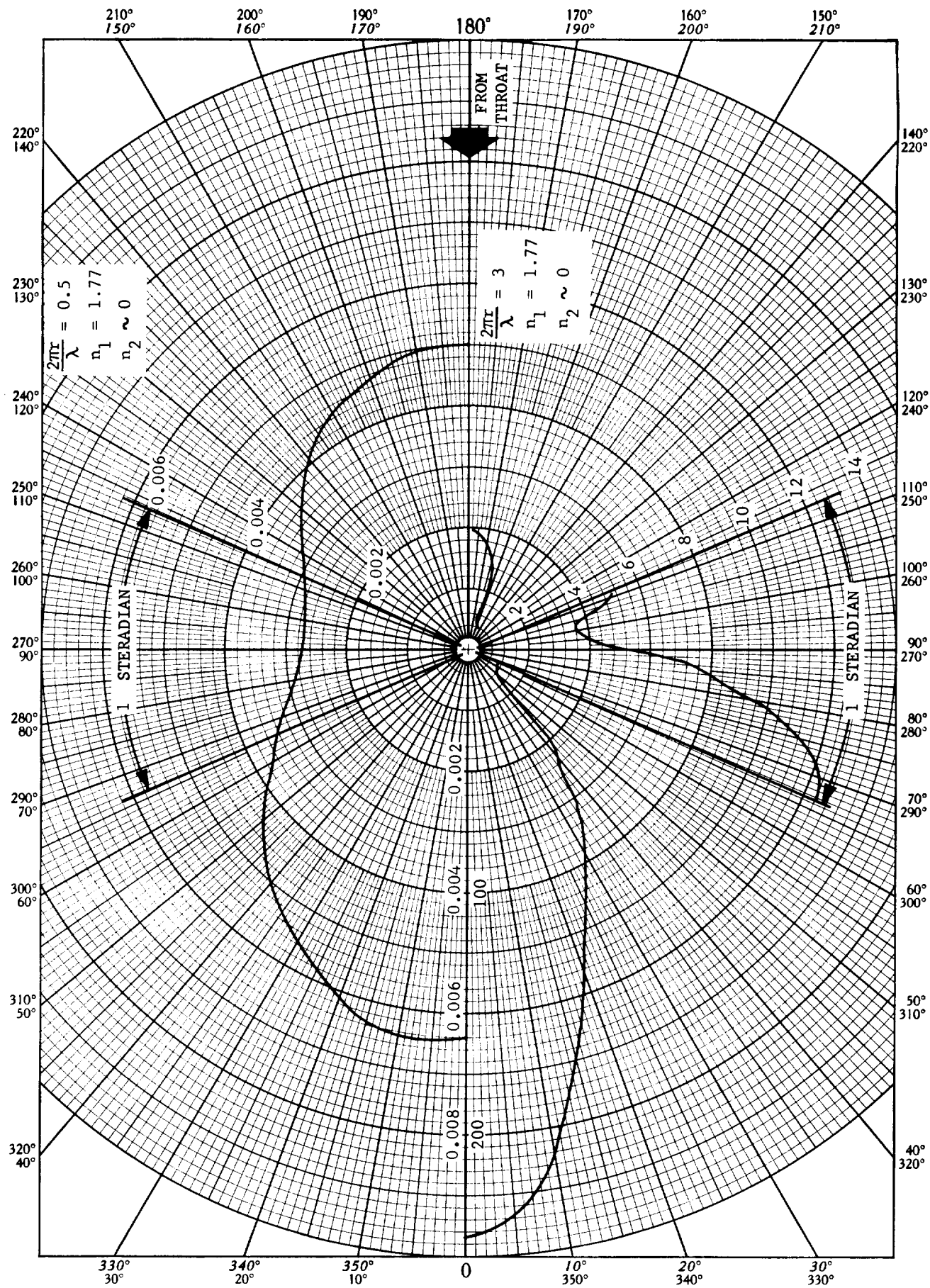


FIGURE 10. POLAR SCATTERING DIAGRAMS FOR COMPUTATION OF \bar{f} : $2\pi r/\lambda = 0.5, 3$

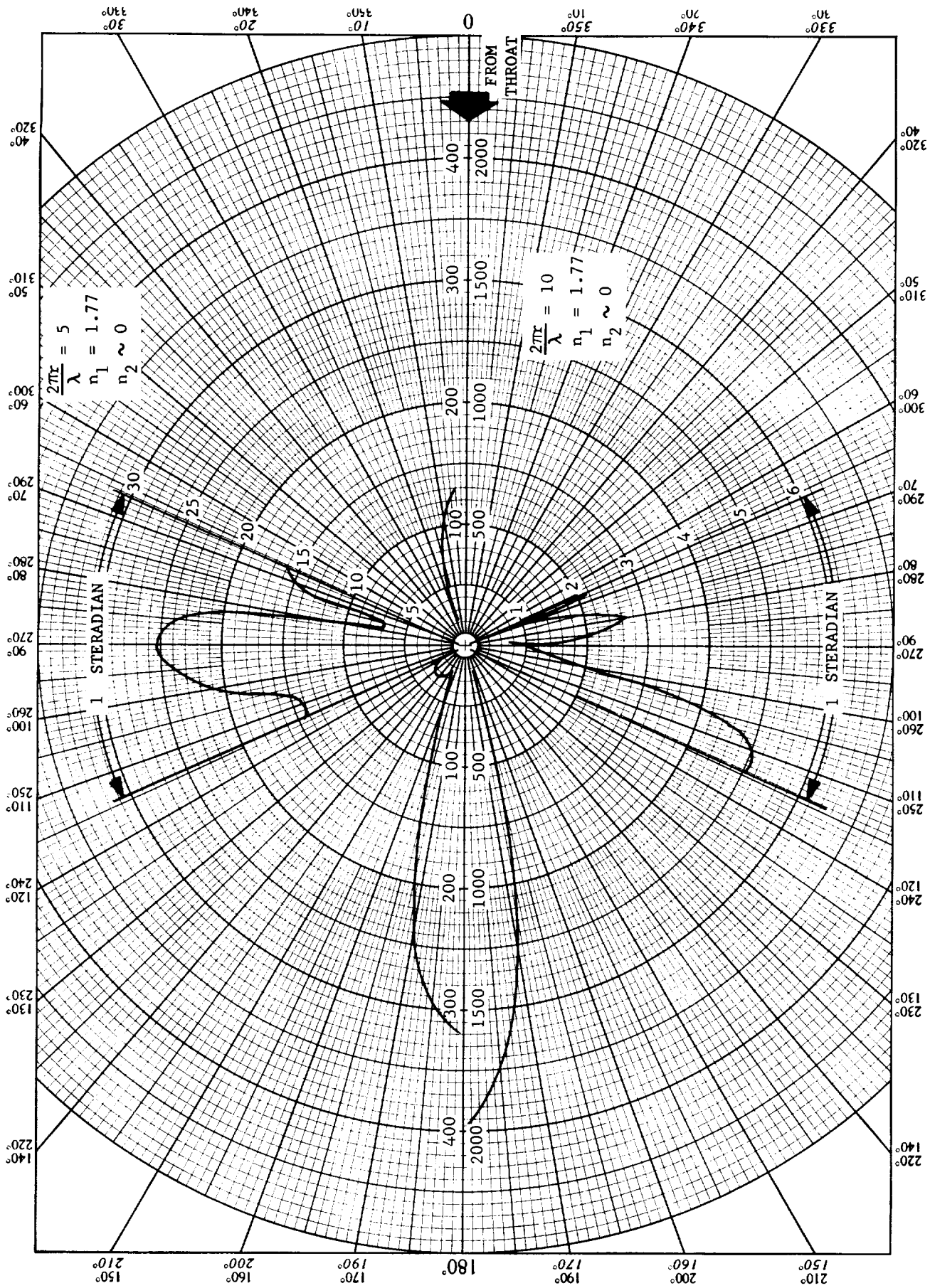


FIGURE 11. POLAR SCATTERING DIAGRAMS FOR COMPUTATION OF \bar{f} : $2\pi r/\lambda = 5, 10$

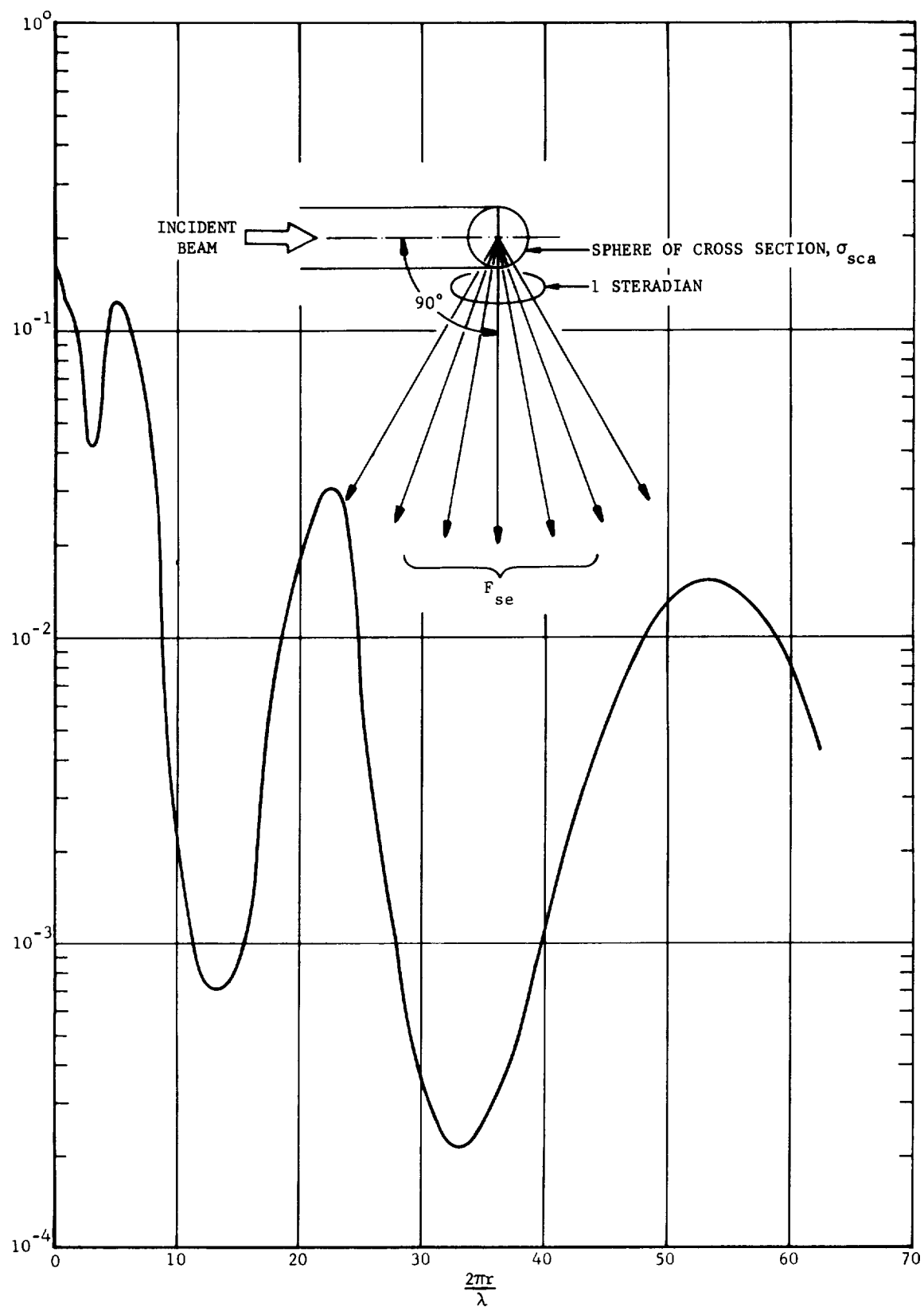


FIGURE 12. FRACTION OF ENERGY INCIDENT ON A SPHERE WHICH IS SCATTERED INTO ONE STERADIAN CENTERED AT 90° TO THE INCIDENT DIRECTION

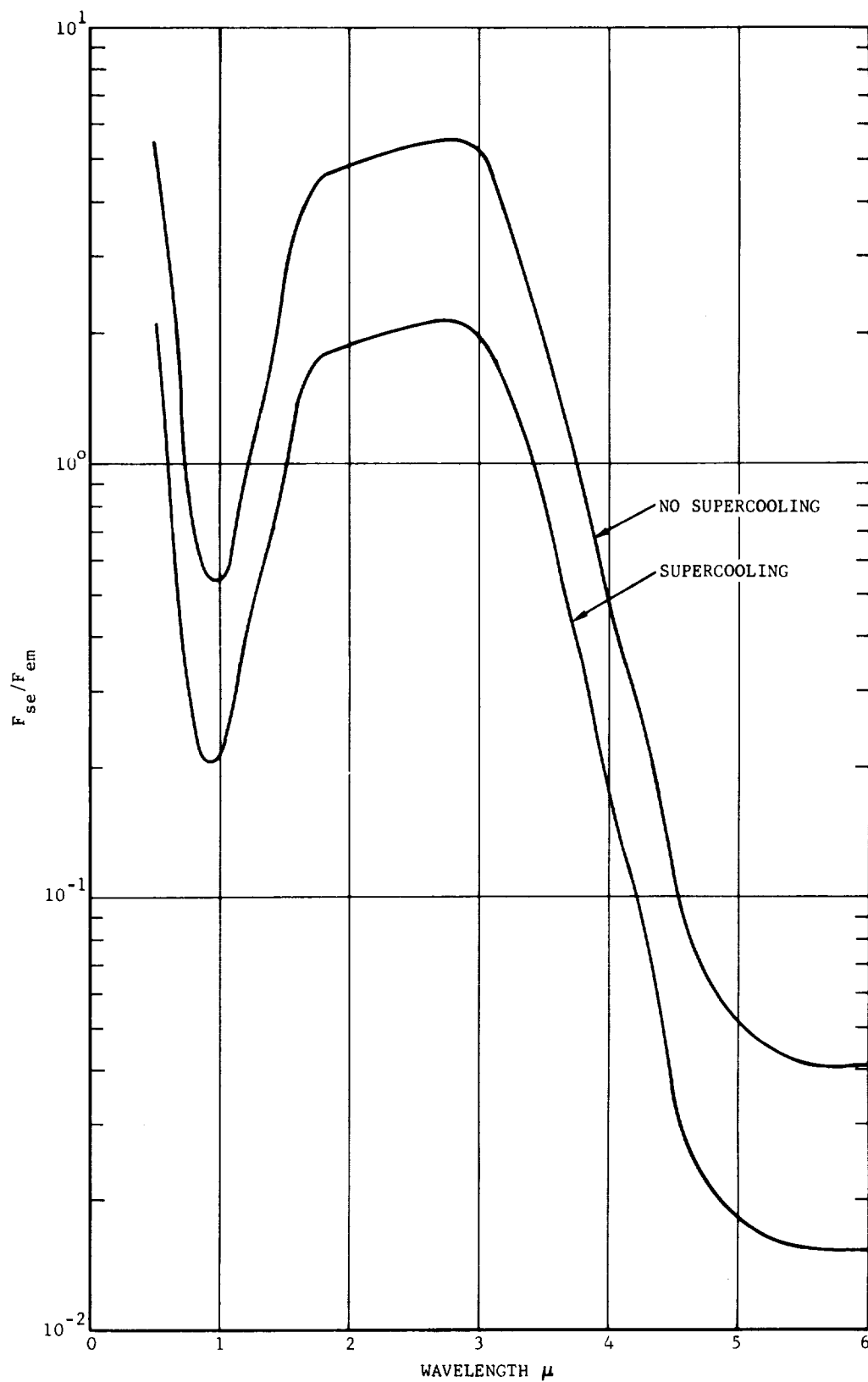


FIGURE 13. RATIO OF SCATTERED LIGHT (SEARCHLIGHT EMISSION) TO THERMAL EMISSION FOR CONDITIONS OF SII ULLAGE MOTOR RADIOMETER MEASUREMENT

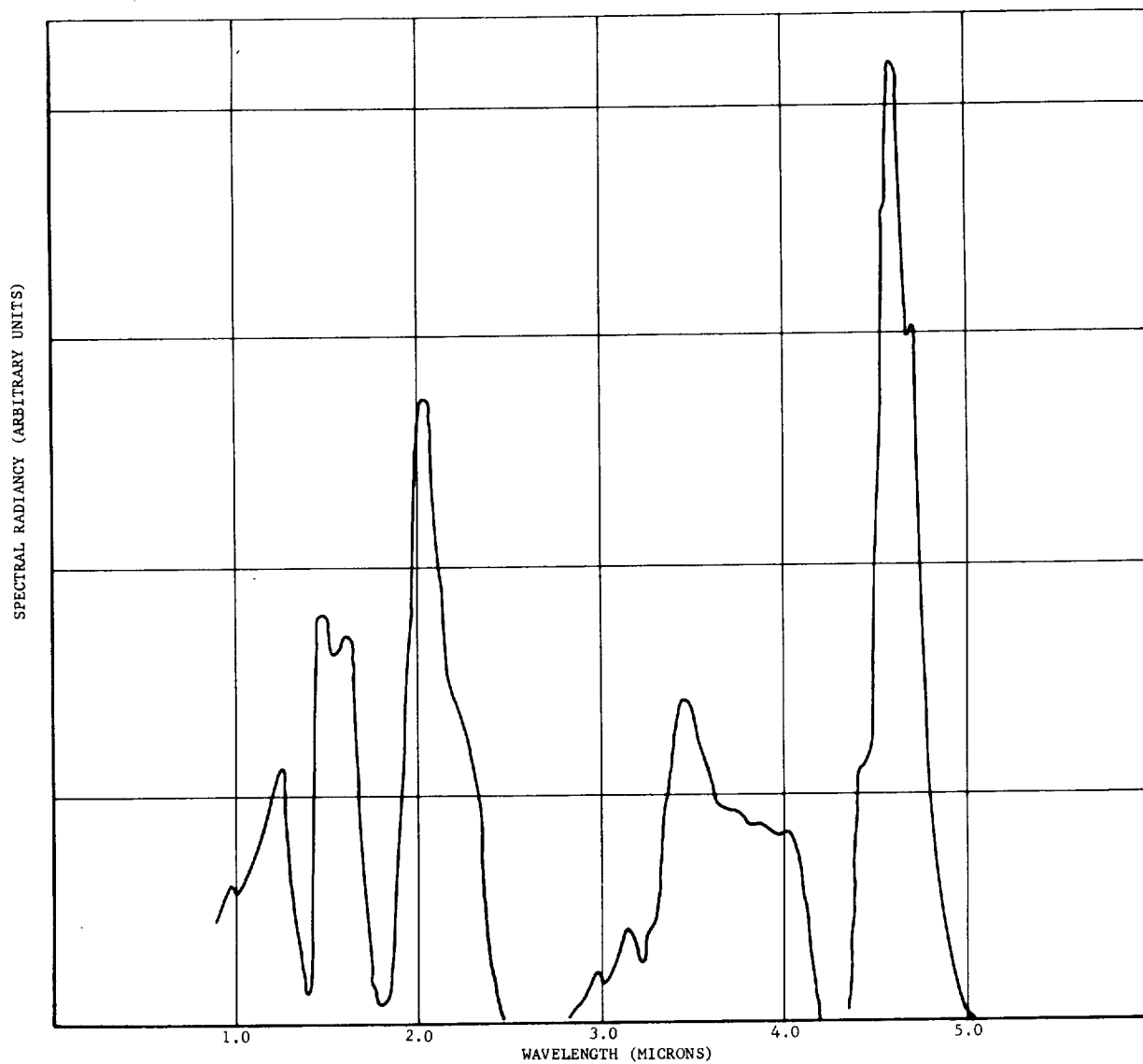


FIGURE 14. FLIGHT SPECTRUM OF SOLID PROPELLANT BOOSTER

SPECTRAL RADIANCE (ARBITRARY UNITS)

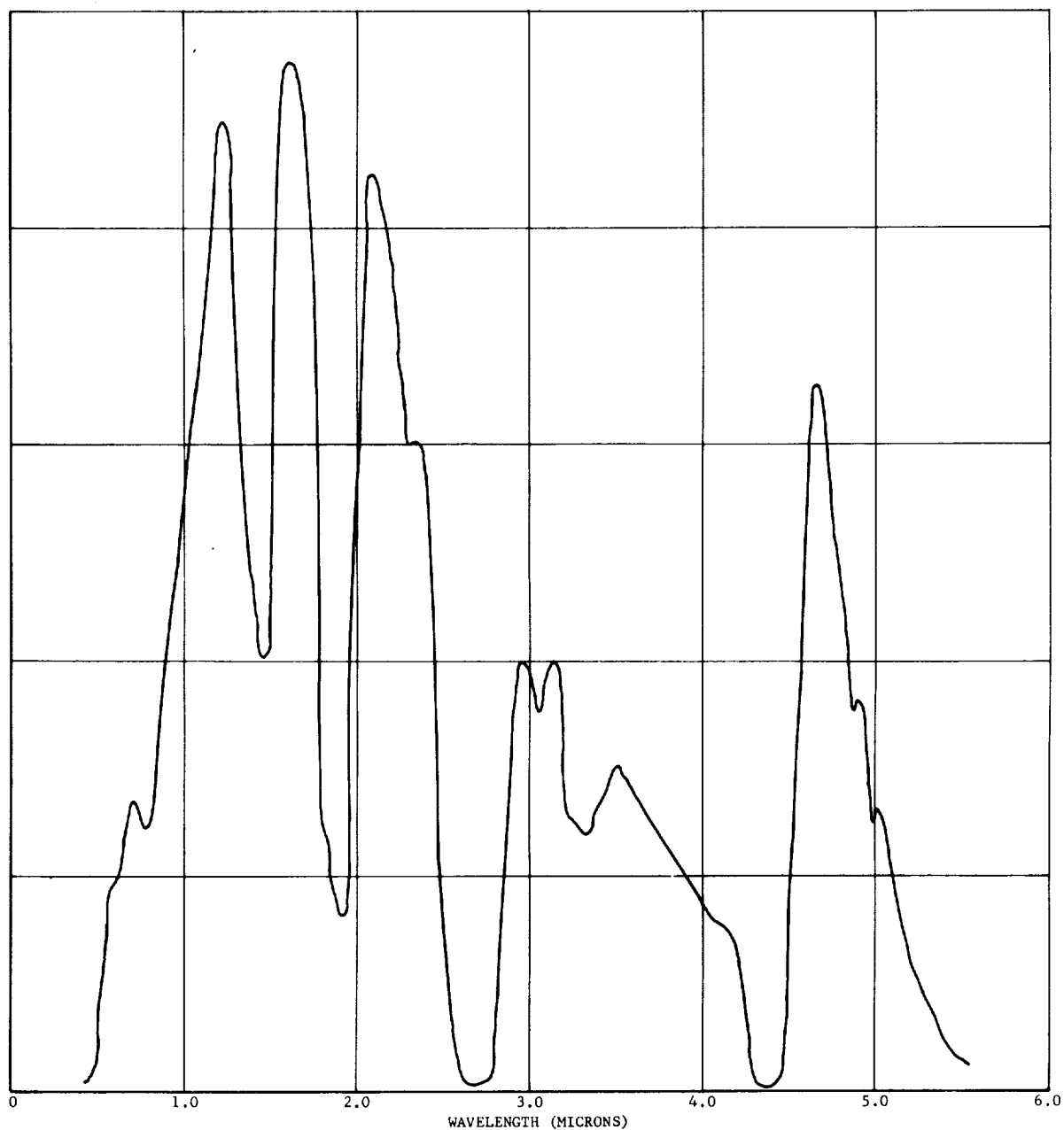


FIGURE 15. GROUND TEST SPECTRUM OF LARGE SOLID PROPELLANT BOOSTER

REFERENCES

1. Morizumi, S. J., and Carpenter, H. J., J. Spacecraft, 1, 501, (1964).
2. Fontenot, J. E., AIAA Journal, 3, 970, (1965).
3. Prozan, R. J., "Development of a Method of Characteristics Solution for Supersonic Flow of an Ideal, Frozen, or Equilibrium Reacting Gas Mixture," Lockheed Missiles and Space Co., LMSC/HREC A782535-A, April 1966.
4. Carlson, D. J., AIAA Journal, 3, 359, 1965.
5. Hill, J. A., and Habert, R. H., "Gasdynamics of High-Altitude Missile Trails," Mithras, Inc., Final Report MC-61-18-R1, January 1963.
6. Kliegel, J., "Gas-Particle Nozzle Flows," Ninth Symposium (International) on Combustion, (Academic Press, Inc., New York, 1963), pp. 811-826.
7. Carlson, D. J., et.al., "A Study of High Altitude Rocket Plume Phenomena (U)," Aeronutronic Publication No. S-2380, December 1963, (SECRET).
8. Carlson, D. J. and Hoglund, R. F., AIAA Journal, 2, 1980 (1964).
9. Hoglund, R. F., ARS Journal, 32, 662 (1962).
10. Carlson, D. J., "Emittance of Condensed Oxides in Solid Propellant Combustion Products," Tenth Symposium (International) on Combustion, (The Combustion Institute, Pittsburgh, 1965), pp. 1413-1424.
11. van de Hulst, H. L., "Light Scattering by Small Particles," (John Wiley and Sons, Inc., New York, 1957).

12. Aeronutronic Computer Program "Mie Scattering," Computer Library No. RP08F.
13. Aeronutronic Computer Program "Punch," Computer Library No. HT40F.
14. Morin, F., Phys. Rev., 83, 1005 (1951).
15. Tannhauser, J. Phys. Chem. Solids, 23, 25 (1962).
16. Bailey, F. C., J. Appl. Phys., 31S, #5, 39S (1960).
17. Morin, F. J., Phys. Rev., 93, 1195 (1954).
18. Banks, E., Riederman, N. H., Schleuning, H. W., and Silber, L. M., Trans. 7th Vacuum Symp., 1960 (Pergamon, N.Y.), p. 297.
19. Waldron, R. D., Phys. Rev., 99, 1727 (1955).
20. McDevitt, N. T., and Baun, W. L., Spectrochim. Acta, 20, 799 (1964).
21. Vratny, F., Dilling, M., Gugliotta, F., and Rao, C.N.R., J. Sci. & Ind. Res. (India) 20, 590 (1961).
22. Lewis, D. C. and Westwood, W. D., Canad. J. Phys., 42, 2367 (1964).
23. Holland, L., "Vacuum Depositions of Thin Films," (Wiley, New York, 1956).
24. Landolt-Bornstein, "Zahlenwerte und Funktionen aus Naturwissenschaften und Technik," Neuserie, Band 2, Achte Teil (Springer, Berlin, 1961).
25. Handbook of Chemistry and Physics, Edited by Hodgman, C. D., Weast, R. L., and Selby, S. M., Chemical Rubber Publishing Co., Cleveland, Ohio.
26. Bartky, C. D., and Bauer, E., J. Spacecraft, 3, 1523 (1966).
27. Gryvnak, D. A., and Burch, D. C., J. Opt. Soc. Am., 55, 625 (1965).
28. Adams, J. M., and Colucci, S. E., "The Spectroscopic Measurement of Gas and Particle Temperature in Metallized Propellant Combustion," Paper S66-175, ICRPG/AIAA Solid Propellant Conference, Washington, D.C., July 18-21, 1966.
29. Bauer, E., and Carlson, D. J., J. Quant. Spectrosc. Radiat. Transfer, 4, 363 (1964).
30. Chandrasekhar, S., "Radiative Transfer," (Dover Publications, New York, 1960).

31. Hanaker, H. C., "Radiation and Heat Conduction in Light Scattering Material," Phillips Research Reports, 2, pp. 55-67, 103-111, 112-125, 420-425 (1947).
32. Ferriso, C. C., Ludwig, C. B., and Acton, J. Opt. Soc. Am. 56, 171 (1966).
33. Ferriso, C. C., and Ludwig, C. B., J. Chem. Phys. 41, 1668 (1964).
34. Ludwig, C. B., Ferriso, C. C., and Abeyta, C. N., J. Quantit. Spectr. and Radiat. Transfer 5, 281 (1965).
35. Ferriso, C. C., and Ludwig, C. B., Appl. Opt. 3, 1435 (1964).
36. Stull, Robert V., and Plass, Gilbert, N., J. Opt. Soc. Am. 50, 1279 (1960).
37. Rochelle, W. C., "Modified SIC Ordnance Disconnect Heating Analysis and SII Ullage Motor Test Results," NASA/MFSC Memorandum for File, AT-20-65, Nov. 23, 1965.
38. Reardon, John, Hayes Engineering, Private Communication to W. C. Kuby.
39. Rochelle, W. C., Private Communication to W. C. Kuby.
40. Rochelle, W. C., Private Communication to W. C. Kuby.
41. ———, "Research on Base Heating of Rocket Motor Vehicles Using Shock Tube Techniques," Progress Report No. 20 on Cornell Aeronautical Lab Project No. HM-2045-Y Contract No. NAS 8-20027, Sept. 1966.
42. Baier, R. W., Byron, S. R., and Armour, W. H., "Application of the Bray Criterion for Predicting Atomic Recombination Effects in Propulsion Systems," Western States Section, The Combustion Institute, Second Conference on Kinetics, Equilibria, and Performance of High Temperature Systems, Los Angeles, California, 16-18 April, 1962.
43. Leavitt, B. P., J. Chem. Phys., 42, 1038 (1965).
44. Cottrell, T. L., and McCoubrey, J. C., Molecular Energy Transfer in Gases, Butterworths, London (1961).
45. Weber, M. J., and Deutsch, T. F., IEEE J. Quantum Elec. QE-2, 369 (1966).

46. Jacobs, D. B., "Launch Vehicle Aerothermodynamic Design Assurance," Doc. No. D5-15441-2, Boeing Co. Space Division Launch Systems Branch, November 30, 1966.
47. Rochelle, W. C., "Theoretical and Experimental Investigation of Heating from Saturn Solid Propellant Rocket Exhausts," Paper No. 66-653, AIAA Second Propulsion Joint Specialist Conference, Colorado Springs, Colorado, June 16, 1966.
48. ———, Final Report on Contract NAS 8-11850, "Heat Transfer and Ablation Rate Measurement in Saturn SII Ullage Motor Exhaust Plume," Heat Technology Lab. Inc. Report No. HTL-TR-31, July 22, 1966.
49. Fay, J. A., and Riddell, F. R., J. Aero. Sci., 25, 73, (1958).